

The Mean Star Formation Rate of X-ray selected Active Galaxies and its Evolution from $z \sim 2.5$: Results from PEP-Herschel [★]

D. J. Rosario¹, P. Santini^{1,2}, D. Lutz¹, L. Shao¹, R. Maiolino², D. M. Alexander³, B. Altieri⁴, P. Andreani^{5,6}, H. Aussel⁷, F. E. Bauer^{8,9}, S. Berta¹, A. Bongiovanni^{9,10}, W. N. Brandt¹¹, M. Brusa¹, J. Cepa^{10,12}, A. Cimatti¹³, T. J. Cox¹⁴, E. Daddi⁷, D. Elbaz⁷, A. Fontana², N. M. Förster Schreiber¹, R. Genzel¹, A. Grazian², E. Le Floch⁷, B. Magnelli¹, V. Mainieri⁵, H. Netzer¹⁵, R. Nordon¹, I. Pérez García^{10,12}, A. Poglitsch¹, P. Popesso¹, F. Pozzi¹², L. Riguccini⁷, G. Rodighiero¹⁶, M. Salvato^{17,1}, M. Sanchez-Portal⁴, E. Sturm¹, L. J. Tacconi¹, I. Valtchanov⁴, and S. Wuyts¹

¹ Max-Planck-Institut für Extraterrestrische Physik (MPE), Postfach 1312, 85741 Garching, Germany.

² INAF - Osservatorio Astronomico di Roma, via di Frascati 33, 00040 Monte Porzio Catone, Italy.

³ Department of Physics, Durham University, South Road, Durham, DH1 3LE, UK.

⁴ European Space Astronomy Centre, Villafranca del Castillo, Spain.

⁵ ESO, Karl-Schwarzschild-Str. 2, D-85748 Garching, Germany.

⁶ INAF-Osservatorio Astronomico di Trieste, via Tiepolo 11, 34131 Trieste, Italy.

⁷ Laboratoire AIM, CEA/DSM-CNRS-Université Paris Diderot, IRFU/Service d'Astrophysique, Bât.709, CEA-Saclay, 91191 Gif-sur-Yvette Cedex, France.

⁸ Pontificia Universidad Católica de Chile, Departamento de Astronomía y Astrofísica, Casilla 306, Santiago 22, Chile.

⁹ Space Science Institute, 4750 Walnut Street, Suite 205, Boulder, CO 80301, USA

¹⁰ Instituto de Astrofísica de Canarias, 38205 La Laguna, Spain.

¹¹ Department of Astronomy and Astrophysics, 525 Davey Lab, Pennsylvania State University, University Park, PA 16802, USA.

¹² Departamento de Astrofísica, Universidad de La Laguna, Spain.

¹³ Dipartimento di Astronomia, Università di Bologna, Via Ranzani 1, 40127 Bologna, Italy.

¹⁴ Carnegie Observatories, 813 Santa Barbara Street, Pasadena, CA, 91101, USA

¹⁵ School of Physics and Astronomy, Tel Aviv University, 69978 Tel Aviv, Israel.

¹⁶ Dipartimento di Astronomia, Università di Padova, Vicolo dell'Osservatorio 3, 35122 Padova, Italy.

¹⁷ IPP-Max-Planck-Institut für Plasmaphysik, Boltzmannstrasse 2, D-85748, Garching, Germany.

Received ; accepted

ABSTRACT

We study relationships between star-formation rate (SFR) and the accretion luminosity and nuclear obscuration of X-ray selected Active Galactic Nuclei (AGNs) using a combination of deep far-infrared (FIR) and X-ray data in three key extragalactic survey fields (GOODS-South, GOODS-North and COSMOS), as part of the PACS Evolutionary Probe (PEP) program. The use of three fields with differing areas and depths enables us to explore trends between the global FIR luminosity of the AGN hosts and the luminosity of the active nucleus across 4.5 orders of magnitude in AGN luminosity (L_{AGN}) and spanning redshifts from the Local Universe to $z = 2.5$. Using imaging from the Herschel/PACS instrument in 2-3 bands, we combine FIR detections and stacks of undetected objects to arrive at mean fluxes for subsamples in bins of redshift and X-ray luminosity. We constrain the importance of AGN-heated dust emission in the FIR and confirm that the majority of the FIR emission of AGNs is produced by cold dust heated by star-formation in their host galaxies.

We uncover characteristic trends between the mean FIR luminosity (L_{60}) and accretion luminosity of AGNs, which depend both on L_{AGN} and redshift. At low AGN luminosities, accretion and SFR are uncorrelated at all redshifts, consistent with a scenario where most low-luminosity AGNs are primarily fueled by secular processes in their host galaxies. At high AGN luminosities, a significant correlation is observed between L_{60} and L_{AGN} , but only among AGNs at low and moderate redshifts ($z < 1$). We interpret this observation as a sign of the increasing importance of major-mergers in driving both the growth of super-massive black holes (SMBHs) and global star-formation in their hosts at high AGN luminosities. We also find evidence that the enhancement of SFR in luminous AGNs weakens or disappears at high redshifts ($z > 1$) suggesting that the role of mergers is less important at these epochs. At all redshifts, we find essentially no relationship between L_{60} and nuclear obscuration across five orders of magnitude in obscuring Hydrogen column density (N_H), suggesting that various mechanisms are likely to be responsible for obscuring X-rays in active galaxies.

We discuss a broad scenario which can account for these trends: one in which two different modes of AGN fueling operate in the low- and high-luminosity regimes of SMBH accretion. We postulate that the dominant mode of accretion among high-luminosity AGNs evolves with redshift. Our study, as well as a body of evidence from the literature and emerging knowledge about the properties of high redshift galaxies, supports this scenario.

Send offprint requests to: D.J. Rosario e-mail: rosario@mpe.mpg.de

[★] *Herschel* is an ESA space observatory with science instruments provided by European-led Principal Investigator consortia and with important participation from NASA.

1. Introduction

A number of different lines of evidence suggest that a close relationship exists between the growth of supermas-

sive black holes (SMBHs) and their host galaxies. There are now well-established and tight correlations between the properties of nuclear supermassive black holes (SMBHs) and the spheroids of their host galaxies (Magorrian et al. 1998; Ferrarese & Merritt 2000; Ferrarese et al. 2001; Marconi & Hunt 2003; Ferrarese & Ford 2005; Gültekin et al. 2009; Gebhardt et al. 2000; Tremaine et al. 2002). The strong evolution in the cosmic star-formation rate (SFR) density (e.g., Hopkins & Beacom 2006) is also reflected in the evolution of the number density of bright Quasi-stellar Objects (QSOs) and the cosmic SMBH accretion rate density since $z \sim 3$ (Boyle & Terlevich 1998; Ueda et al. 2003; Croom et al. 2004; Silverman et al. 2008; Aird et al. 2010; Assef et al. 2011). In addition, AGNs, like star-forming galaxies (Fontanot et al. 2009), display a form of ‘down-sizing’, by which the population that dominates either nuclear or star-forming activity moves to systems at lower luminosities or masses towards later epochs (Cowie et al. 2003; Fiore et al. 2003; Hasinger et al. 2005; Bongiorno et al. 2007).

Observational studies of the relationship between host star-formation and AGN activity are an essential test of the degree and importance of galaxy-SMBH co-evolution scenarios. Traditionally, such studies of star-formation in AGNs have concentrated on interesting subsamples, usually luminous or rare types, such as bright QSOs, radio-loud AGNs or bright local Seyfert galaxies. Many of these types of AGNs are associated with on-going starbursts (Rowan-Robinson 1995; Haas et al. 1998; Omont et al. 2003; Priddey et al. 2003; Jahnke et al. 2004; Shi et al. 2005; Schweitzer et al. 2006; Netzer et al. 2007; Greene et al. 2009). In general, one finds clear star-formation signatures in a sizable fraction of bright QSOs (as much as 80%, depending on selection), with some reaching infrared (IR) luminosities placing them in the ultra-luminous IR galaxy (ULIRG) regime (e.g., Page et al. 2004; Stevens et al. 2005; Alexander et al. 2008; Coppin et al. 2008). In a similar vein, a significant fraction of ULIRGs/sub-mm galaxies show clear AGN signatures, though not always at the level of QSOs (Sanders et al. 1988; Sanders & Mirabel 1996; Genzel et al. 1998; Canalizo & Stockton 2001). These studies support the notion of a connection between galaxy mergers and black hole growth, but, by themselves, they do not explore star-formation in the bulk of AGNs.

With the advent of large systematic galaxy surveys, several studies have turned to complete, well-defined samples of AGNs selected by multiple means and covering a large dynamic range in AGN luminosity and obscuration. Star formation in these AGN hosts is revealed typically through photometric or spectroscopic signatures at optical or UV wavelengths. Kauffmann et al. (2003) calibrated the star-formation history of emission-line selected AGNs in the local Universe using spectra from Sloan Digital Sky Survey (SDSS) and found that the mean SFR and typical ages of AGN host galaxies are respectively higher and younger than those of inactive galaxies. Post-starburst spectroscopic signatures are also found to be strong in AGN hosts (Wild et al. 2007), while there is evidence in some AGNs that nuclear activity follows a few 100 Myr after a strong starburst (Davies et al. 2007; Wild et al. 2010).

At higher redshifts, multi-wavelength surveys such as GOODS (Dickinson et al. 2003), COSMOS (Scoville et al. 2007) and AEGIS (Davis et al. 2007) played a major role. Silverman et al. (2009), using the SF sensitive [O II] λ 3727 emission line, found wide-spread SF in low and moderate luminosity AGN hosts at levels comparable to inactive galaxies of similar stellar mass. AGN host colors paint a similar picture

(Xue et al. 2010; Rosario et al. 2011). Clustering studies suggest that AGNs are associated more with red or evolved galaxies, rather than the bulk of star-forming galaxies (Coil et al. 2009). These studies generally imply that low-luminosity AGNs are hosted by a special category of galaxy that is quite evolved but still forming stars. Since SFR correlates quite strongly with stellar mass (Noeske et al. 2007; Daddi et al. 2007; Santini et al. 2009) and AGN hosts are preferentially hosted by massive galaxies (Alonso-Herrero et al. 2008), stellar mass selection effects can bias any inferences about SF in AGN hosts (Silverman et al. 2009; Xue et al. 2010; Rosario et al. 2011). When taken into account, active and inactive galaxies are found to be quite similar in their average SF properties.

A caveat of most studies of star-formation in AGN hosts is that they tend to concentrate on low and moderate luminosity AGNs. This is because the emission of the active nucleus can be a strong contaminant of SF tracers at optical and UV wavelengths. Together with the difficulties stemming from differential dust obscuration and reddening between nuclear and galaxy emission, this makes it next to impossible to accurately determine SF properties of luminous AGNs using these data. Tracers in the IR are useful since extinction is rarely a major issue at these wavelengths (except around the 10 μ m Si absorption feature). The IR continuum comes primarily from reprocessed short wavelength radiation and the total IR luminosity (generally integrated over the range of 8-1000 μ m) is considered to be a good calorimeter of the total bolometric output of both AGNs and SF systems. Since the mid-infrared (MIR) has traditionally been more accessible to observation from early generations of ground and space-based instruments, several studies of SF in AGNs have been based on the measurement of the prominent PAH emission features that are excited in star-forming environments (Netzer et al. 2007; Lutz et al. 2008; Shi et al. 2009). QSOs frequently show stronger PAH features than typical inactive galaxies, though evolution in the properties of the massive galaxy population was generally not taken into account in these studies. Another limitation is that MIR spectroscopy, on which PAH measurements depend, is only sensitive enough for rather IR-bright galaxies, which are not representative of the broad population of AGN hosts.

Wide area galaxy surveys from the new Herschel Space Observatory (Pilbratt et al. 2010) have opened up the ability to carefully measure the rest-frame far infrared (FIR) continuum luminosity of distant galaxies and AGNs. Several studies show that the FIR continuum is the best and least contaminated tracer of SFR in massive galaxies, which are dusty enough for most SF luminosity to be reprocessed into the FIR. In a first study of X-ray selected AGNs in the GOODS-N field, Shao et al. (2010) found that the mean relationship between the L_{AGN} and global host galaxy SF is a function of the accretion luminosity, such that luminous AGNs show a SF- L_{AGN} connection that is absent in lower luminosity systems. Using a similar approach, Mullaney et al. (2012), using deeper FIR imaging in both GOODS fields, find that the mean SFRs of X-ray sources is indistinguishable from those of typical inactive star-forming galaxies, though the study only concentrated on low to moderate luminosity AGNs. Alternatively, Hatziminaoglou et al. (2010) find that FIR luminosity is correlated with AGN luminosity over many orders of magnitude in both quantities, at apparent odds with aspects of both previous results.

Many of the differences between these works can be reconciled by studying the FIR properties of a broad sample of AGNs across many epochs. We present the largest study to-date of the mean SF properties of AGNs, in terms of the range of accretion

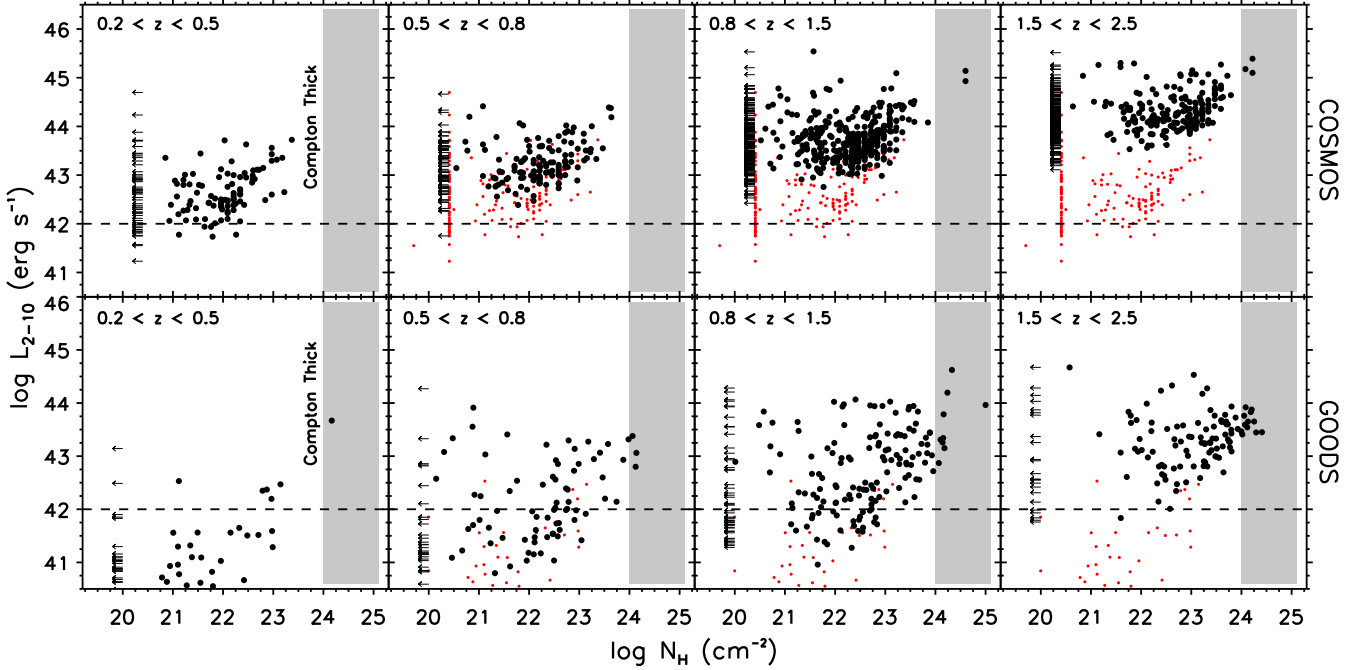


Fig. 1. Rest-frame 2-10 keV (hard band) X-ray luminosity L_X vs. hydrogen obscuring column N_H for X-ray sources in this study. The upper four panels show sources in COSMOS, while the lower panels show sources from both GOODS fields combined. Each panel is for a different bin in redshift, increasing left to right. In the three higher redshift bins, the location of the X-ray sources from the lowest ($0.2 < z < 0.5$) bin are shown for reference as small red points, to clearly bring out the redshift trends in the sample. Sources with N_H consistent with only Galactic obscuration are shown as left-pointing arrows. The fiducial limit of $L_X = 10^{42}$ erg s^{-1} used to define a clean AGN sample (employed in §4.3) is shown by a dashed line. The nominal Compton thick regime of X-ray obscuration ($N_H > 10^{24}$ cm^{-2}) is shown as a shaded region in each panel.

luminosity (5.5 orders of magnitude), SFR and redshift (Local to $z = 2.5$). This is the second paper of a series that combines deep FIR images and the best current X-ray analysis in multiple deep fields to determine the SF characteristics of a large sample of AGNs spanning the redshifts $0.2 < z < 2.5$. Using techniques of FIR stacking, we have constrained the mean FIR luminosities for active galaxies across redshift, AGN luminosity, obscuration and host mass. In the first paper of the series (Santini et al. 2012), we studied the mean SFR of AGN hosts as function of stellar mass and redshift, finding a slight enhancement compared to inactive galaxies with the same stellar mass distribution. In this work, we build on early work from our team (Shao et al. 2010) and uncover trends with AGN luminosity and obscuration. The paper is organised as follows: §2 describes the datasets used and outlines our methods (which are detailed in the Appendix), §3 deals with AGN emission in the FIR as a source of contamination, §4 outlines our main trends, fits and tests for biases. In §5, we discuss our results in the context of galaxy evolution.

We assume a standard Λ -CDM Concordance cosmology, with $H_0 = 70$ $km\ s^{-1}\ Mpc^{-1}$.

2. Datasets, Sample Selection and Methods

This work exploits deep X-ray and FIR imaging, as well as extensive ancillary data, in three well-studied extragalactic fields: GOODS-South, GOODS-North and COSMOS. The depth of the two GOODS fields in the X-ray, FIR and several other bands is essential to probe faint and high-redshift AGNs. The shallower, wide-area COSMOS field provides us with good statistics among the more luminous sources, which are rare in the smaller GOODS fields.

2.1. X-ray catalogs

Detailed X-ray point source catalogs were compiled for all three fields. These provide rest-frame X-ray luminosities and obscuring columns, source classification, optical associations and redshifts. Where possible, spectroscopic redshifts were used. In the absence of these, photometric redshifts specifically suited for AGN hosts, based on optimised AGN or hybrid templates, were compiled.

For GOODS-S we used the Luo et al. (2008) catalog from the 2 Msec Chandra Deep Field-South imaging program. A small set of new redshifts from recent spectroscopic efforts (Silverman et al. 2010) were included, and photometric redshifts were compiled from the work of Luo et al. (2010).

For GOODS-N we used the 2 Msec Chandra Deep Field-North catalog of Alexander et al. (2003) and an updated version of the classification into AGN and other types of X-ray sources compiled by Bauer et al. (2004) (see also Shao et al. 2010).

Finally, for COSMOS, we used the XMM-Newton catalog compiled by Cappelluti et al. (2009) and the X-ray optical associations and derived properties presented in Brusa et al. (2010) in its updated version, which includes new redshifts from ongoing (mostly DEIMOS/KECK) spectroscopic campaigns and a few changes in the published redshifts and/or spectroscopic classifications from a re-analysis of the data (Mainieri et al. 2011). Photometric redshifts are as derived by Salvato et al. (2009).

Rest-frame X-ray luminosities in the hard band (2-10 keV) were estimated for all our AGNs, using spectral fits for X-ray sources with sufficient counts or using scalings based on hardness ratios for faint X-ray sources. Where possible, the Hydrogen column densities of obscuring gas towards the X-ray

sources (N_H) were also estimated. The X-ray luminosities were then corrected to account for the level of obscuration, yielding absorption-corrected hard-band luminosities (L_X hereafter). It must be kept in mind that N_H estimates, especially for obscured AGNs at higher redshifts, can be fairly uncertain. X-ray luminosities in the hard band, however, are generally more secure, though, of course, for heavily obscured sources, the uncertainty in N_H will translate into a greater uncertainty in L_X .

In this work, we consider the properties of all X-ray sources with L_X greater than 10^{41} erg s $^{-1}$. At the low-luminosity end ($L_X < 10^{42}$ erg s $^{-1}$), there may be some contamination from very luminous star-bursts where soft-band emission from star-formation related processes (SNe, high-mass X-ray binaries) can contaminate the sample. Since we study trends with AGN luminosity in our main analysis, we can easily test for the importance of such starburst contamination in our sample. In general, we do not find that low luminosity X-ray sources are more strongly star-forming than moderate luminosity sources, except in the redshift range 0.2 – 0.5. We account for such effects in our analysis.

A sense of the differing depths of the X-ray data in the three fields may be gained from Fig. 1, which plots L_X against the obscuring column N_H for the X-ray sources from the three catalogs used in this analysis. We split the sample into a set of 4 redshift bins: $0.2 < z < 0.5$, $0.5 < z < 0.8$, $0.8 < z < 1.5$ and $1.5 < z < 2.5$. The fields are complementary in terms of their X-ray properties: the deep GOODS fields allow a good sampling of faint AGN, while in the large-area COSMOS field we probe the rarer and more powerful sources.

The X-ray sources also display strong trends of N_H with redshift, especially in the COSMOS field. This is governed mostly by selection effects (Tozzi et al. 2006). At all redshifts, a substantial fraction of AGNs have absorbing columns consistent with no intrinsic absorption (i.e. only absorption by gas in our own Galaxy). Towards higher redshifts, the rest-frame soft X-ray energies redshift out of the detection bands of both Chandra and XMM-Newton, leading to greatly reduced accuracy in the measurement of N_H in weakly absorbed sources, as well as smaller range of estimated N_H values from most spectral fitting methods. This explains the large number of sources clustered around $\log N_H = 20.5$ cm $^{-2}$ in the upper panels. In addition, absorbed low-luminosity AGNs are badly incomplete in flux-limited X-ray surveys, leading to an apparent correlation between N_H and L_X , which can be seen most clearly in the high redshift panels of Fig. 1. While the span of L_X in any given redshift bin is fairly broad, the span of N_H that we can probe in a bin can be quite limited.

2.2. PACS Imaging and catalogs

Our FIR data come from observations by the PACS instrument (Poglitsch et al. 2010) on board the Herschel Space Observatory, as part of the PACS Evolutionary Probe (PEP, Lutz et al. 2011) survey. Observations of GOODS-S were carried out in all three PACS bands (70, 100 and 160 μ m), while the other two fields were only observed in the two long wavelength bands. We made use of PACS catalogs extracted using prior knowledge of the positions and fluxes of sources detected in deep archival IRAC 3.6 μ m and MIPS 24 μ m imaging in these fields. This allows us to deblend PACS sources in images characterized by a large PSF, especially in crowded fields, and improve the completeness of faint sources at the detection limit. Fluxes in GOODS-S reach 1.1, 1.2 and 2.4 mJy at 3σ in the 70, 100 and 160 μ m bands respectively. In the other two fields the 3σ flux limit at

100/160 μ m is 3.0/5.7 mJy in GOODS-N and 5.0/10.2 mJy in COSMOS (Berta et al. 2011). Detailed information on the PEP survey, observed fields, data processing and source extraction may be found in Lutz et al. (2011).

X-ray sources were matched to PACS sources through their optical counterparts. In most cases, a robust crossmatch could be made between the optical counterpart of an X-ray source and a 24 μ m source in the catalogs used to extract PACS fluxes. In the few cases where the crossmatches were not robust, either due to uncertain associations between optical and 24 μ m sources, or due to multiplicity in a match, we visually examined the matches on the 24 μ m images to verify their quality and discard unreliable matches. The technique used to associate PACS fluxes with optical counterparts could in principle introduce some biases in the determination of the mean FIR luminosity, since AGNs are typically brighter than inactive galaxies at MIR wavelengths (e.g. 24 μ m). In Santini et al. (2012), we show that this bias is unimportant.

2.3. Swift BAT sample

For a comparison to local X-ray selected AGNs, we also compiled an unbiased sample of extremely hard X-ray-selected AGN (15-150 keV band) from the 39 month Palermo Swift-BAT catalog (Cusumano et al. 2009). This sample has also been used in Lutz et al. (2010) and Shao et al. (2010).

From the Swift-BAT catalog, we selected sources classified as Seyferts, LINERs, quasars, and other AGNs. We excluded objects with evidence for a strong non-thermal contribution to the far-infrared (on the basis of the NED SED) or those classified as blazars. In addition, objects at Galactic latitude $|b| < 15$ and objects at redshift $z > 0.3$ were also removed. For the remaining 293 AGNs we used the IRAS Faint Source Catalog 60 μ m detections where available, otherwise we used SCANPI¹ to obtain 60 μ m measurements for faint or individually nondetected objects. We calculated rest-frame 2-10 keV luminosities extrapolating from the BAT fluxes and the redshift, assuming an AGN photon index of 1.8. The sources were averaged in 7 bins of L_X , with sufficient statistics in each bin.

2.4. Methods

AGNs in all three deep fields were divided into four intervals in redshift (0.2-0.5, 0.5-0.8, 0.8-1.5, 1.5-2.5), spanning the epochs where most black hole growth in the Universe has occurred. In each redshift interval, the AGNs were further divided by L_X into five bins (41-42, 42-43, 43-44, 44-45, 45-45.5 in $\log L_X$). An estimate of the mean FIR luminosity (νL_ν at 60 μ m) in each bin was made by combining PACS photometry for FIR detected AGNs and PACS stacks for FIR-undetected AGNs in each field, and then appropriately combining measurements from all fields together for a single measurement per bin (L_{60}). Details of the PACS photometry, stacking, error estimation and methods of combination between and across fields are developed in the Appendix.

3. AGN emission in the FIR

The key results in this work are based on the notion that rest-frame FIR emission is a proxy of SF activity. A number of previous studies support our assumption based on different grounds. Many authors (e.g. Schweitzer et al. 2006; Netzer et al. 2007;

¹ <http://scanpiops.ipac.caltech.edu/applications/Scanpi/index.html>

Lutz et al. 2008) showed a strong correlation between FIR luminosity and SFR tracers, such as PAH emission features, both in local and high redshift bright (L_{AGN}/L_{FIR} up to ~ 10) QSOs. In this section, we explore the degree to which AGN emission may contribute at FIR wavelengths, in particular at $60 \mu\text{m}$.

3.1. Predictions from Models of AGN-heated dust

The nature of emission from AGN-heated dust has been the topic of several theoretical studies (Pier & Krolik 1992; Granato & Danese 1994; Efstathiou & Rowan-Robinson 1995; Nenkova et al. 2002; Fritz et al. 2006; Schartmann et al. 2008). Most models assume that the dust is distributed in a ‘torus’, i.e., a roughly axisymmetric structure with a finite inner radius, determined by the sublimation temperature of the grains. Smooth and clumpy torus geometries models with a range of parameters have been studied in the literature.

A consistent feature of most torus models is a broad peak in the continuum emission at MIR wavelengths with a sharp dropoff beyond a certain break wavelength. The MIR SED shape shows considerable variation in different models, due to silicate emission and absorption features at $10 \mu\text{m}$ which depend on the geometry of the dusty torus and its optical depth in the MIR. The typical FIR SED is smoother and more uniform among most models. However, a small subset of models, characterised by high MIR optical depths (or dust columns) and large torus sizes, peak at fairly long wavelengths, approaching $60 \mu\text{m}$ (Fritz et al. 2006). In such models, the intrinsic IR AGN SED is quite ‘cold’ and a substantial fraction of the reprocessed AGN power can come out in the FIR.

In addition to torus emission, AGN light can also be reprocessed by dust on kpc scales, in the Narrow Line Region (NLR). NLR dust is typically cooler than torus dust and has a longer tail towards FIR wavelengths (Schweitzer et al. 2008; Mor et al. 2009). The relative strength of this component with respect to the torus emission is a function of the covering factor of NLR clouds, which tends to be quite low (~ 0.1 ; Mor et al. 2009), indicating that the NLR contribution to the total AGN IR luminosity is likely to be small.

The theoretical approach of modelers is useful to understand the *possible* range of intrinsic AGN SED shapes. However, the ‘torus’ and extended circumnuclear environment of the SMBH, which governs the intrinsic SED, has only been studied in a few nearby AGNs, due to the limited spatial resolution of MIR and FIR imagers, and little is known of true variations in their geometry and phase structure.

Other works have taken an empirical approach towards calibrating intrinsic AGN SEDs. Such analyses rely on some knowledge of the range of SEDs of star-forming galaxies, which are better constrained from studies of inactive systems. By subtracting IR templates of star-forming systems from SEDs of active galaxies, one may reveal the residual excess which must arise from AGN-heated dust. Adopting this approach, Netzer et al. (2007), in a study of PG QSOs with bolometric luminosities L_{AGN} in the range of 10^{44} - $10^{46.5}$ erg s^{-1} , derive a mean intrinsic AGN SED that shows strong Si emission features and drops rapidly beyond $\sim 20 \mu\text{m}$. The shape of the mean SED does not appear to depend on the level of SF, but does show considerable intrinsic variation from object to object, especially at NIR-MIR wavelengths.

This work was extended recently by Mullaney et al. (2011), which explores intrinsic AGN SEDs in a sample of 11 local low-to-moderate luminosity hard X-ray selected AGNs with low levels of SF. Using a set of 5 templates which encompass most of

the range of star-forming galaxies, they isolate and model the AGN emission using a smooth broken power-law model, with a sharp long-wavelength dropoff modeled as a modified blackbody. The empirical AGN SEDs from Mullaney et al. (2011) show significant intrinsic variation both in MIR and FIR, with some peaking as far red as $50 \mu\text{m}$. The study also uncovers a dependence of SED shape on AGN luminosity, such that more luminous AGNs have, on average, a steeper long-wavelength dropoff than lower luminosity AGNs. The long-wavelength slope of the mean AGN SED from Mullaney et al. (2011) is shallower than that of the mean QSO SED from Netzer et al. (2007), but this could be due to the lower characteristic AGN luminosity of the Mullaney et al. (2011) sample. Having said this, detailed SED modeling of a sample of Type I AGNs, covering a wide range in AGN luminosity and including contributions from NLR dust emission and hot dust from the outer Broad-Line Region, seems to suggest that the steep FIR dropoff in the Netzer et al. (2007) SED applies even to lower luminosity systems and may be more universal (Mor & Netzer 2012). Given the recent nature of the latter paper, we choose in this paper, to use the SEDs of Mullaney et al. (2011) and Netzer et al. (2007), but caution the reader that this suite of SEDs may overestimate the contribution of the AGN at FIR wavelengths.

Mullaney et al. (2011) also compared their empirical AGN SEDs with those predicted from torus models. The empirical SEDs shapes show a much smaller scatter than those of the smooth torus models of Fritz et al. (2006), but are more comparably matched to the expected range of the clumpy torus models of Schartmann et al. (2008). This may arise simply from differences in the range of parameter space explored by the modelers – the latter clumpy models are dependent on expensive 3-D modeling and explore a smaller range of torus sizes and optical depths, while the Fritz et al. (2006) models with the largest variation are those with large sizes and MIR optical depths.

3.2. FIR colors of AGNs and inactive galaxies

A simple approach towards exploring the importance of AGN contamination at FIR wavelengths is to compare the FIR colors of AGNs against the general population of galaxies. The significantly warmer temperatures of AGN-heated dust gives flat or falling SEDs at long IR wavelengths, which leads to bluer FIR colors among galaxies with a substantial AGN component in the FIR.

In the top panels of Fig. 2, we compare IR colors of PACS-detected X-ray AGNs and all PACS-detected galaxies in the COSMOS field in four redshift bins. No explicit selection has been applied to the PACS-detected galaxies in this plot, except that they have a well-defined spectroscopic or photometric redshift. The AGN points are colored by their hard-band X-ray luminosity ($\log L_X$) using a rainbow color stretch from black ($\log L_X = 42.0$ erg s^{-1}) to red ($\log L_X = 45.5$ erg s^{-1}), more than 3.5 orders of magnitude in AGN accretion luminosity. The low end of the L_X range is a luminosity threshold which is popularly used to identify pure AGN samples, while the upper end overlaps the luminosity range of moderately bright QSOs.

The X-axis of Fig. 2 is the $24 \mu\text{m}$ to $160 \mu\text{m}$ color (m_{24-160}), a MIR to FIR flux ratio, sensitive to warm AGN dust emission. At $z \gtrsim 1$, the MIPS $24 \mu\text{m}$ band is also influenced by silicate absorption, while, at $z \gtrsim 2$, PAH emission contributes as well. The FIR $100 \mu\text{m}$ to $160 \mu\text{m}$ color on the Y-axis ($m_{100-160}$) measures the FIR continuum slope, down to the rest-frame $30 \mu\text{m}$ at $z = 2.5$. The flux measurements in these two PACS bands are used to derive the rest-frame $60 \mu\text{m}$ luminosity in all four

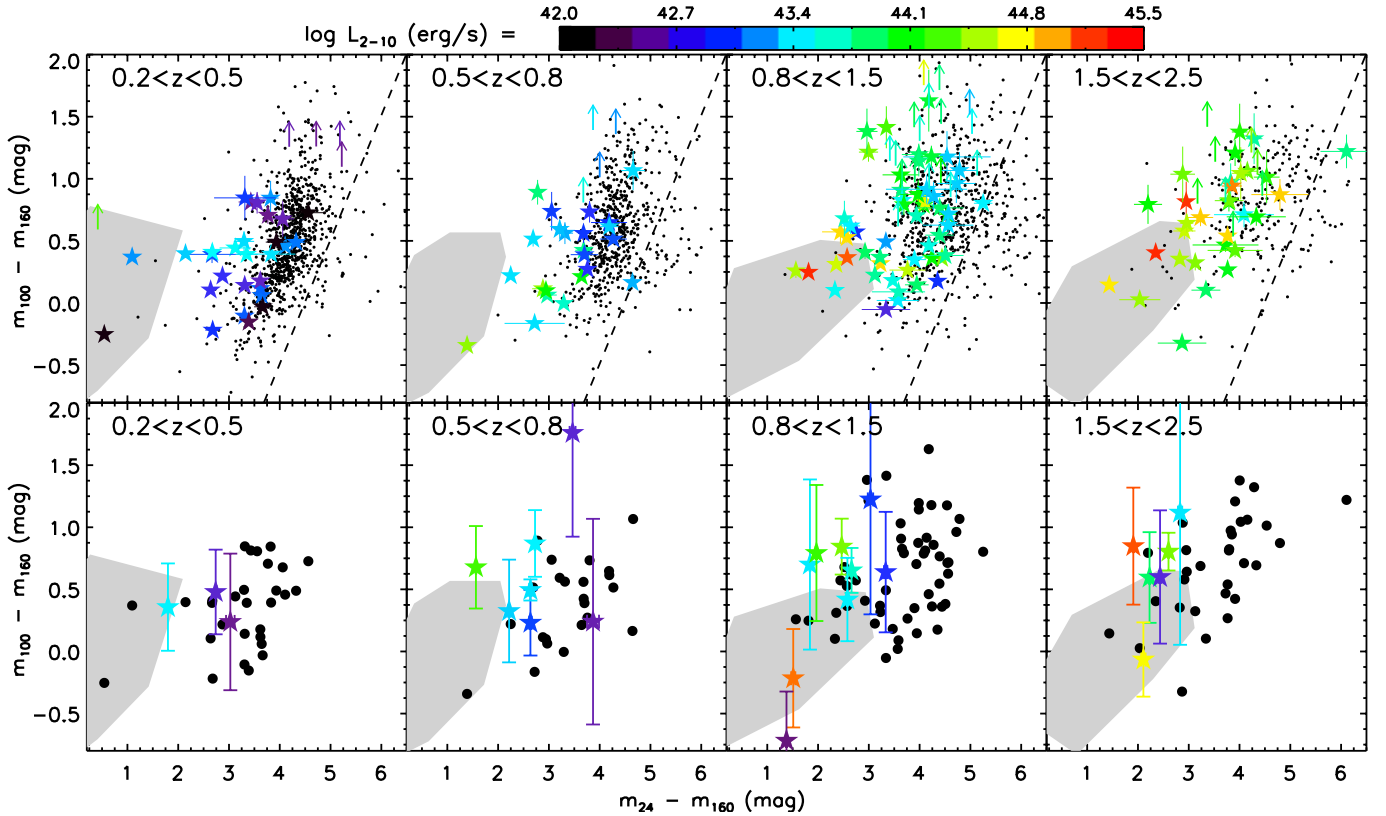


Fig. 2. Observed IR colors of X-ray AGNs plotted in bins of redshift. A MIR flux ratio (the flux at $24\mu\text{m}$ to the flux at $160\mu\text{m}$, expressed as a magnitude) is plotted against an FIR flux ratio (the flux at $100\mu\text{m}$ to the flux at $160\mu\text{m}$, also as a magnitude). The shaded grey regions mark out parts of the diagram occupied by star-forming galaxies with an AGN fraction of $> 50\%$ at rest-frame $60\mu\text{m}$ (§3.2). **Top row panels:** PACS-detected AGNs from the COSMOS field are shown as star-shaped points, with colors that represent their hard-band X-ray luminosity L_X (shown in the color bar at top). The small black dots are all galaxies that are detected in the COSMOS PACS maps in the same redshift bins. Objects with colors right and below the dashed line are unlikely to be detected because of the photometric limits of the MIR and FIR catalogs. **Bottom row panels:** Stacked measurements for PACS-undetected AGNs from all three fields are shown as star-shaped points, colored by L_X . For reference, the large black points show the locations of PACS-detected COSMOS AGNs (the same as the colored points in the top panels). PACS-undetected AGNs have, on average, warmer IR colors and may be more AGN dominated in the FIR.

redshift bins. Therefore, understanding the level of contamination from AGN light in these bands is particularly relevant to the later discussion on FIR trends with AGN luminosity. Both colors are in units of magnitudes; therefore, smaller values (bluer colors) imply systematically warmer SEDs. We will use the term ‘warmer’ to refer to bluer IR colors to avoid any confusion with the colors used in the plotting symbols.

Since the PACS bands probe different rest-frame wavelengths with redshift, we break the sample into our four standard redshift bins to reduce the effect of k-corrections.

From the Figure, one may notice that the AGNs on average show warmer m_{24-160} than normal (i.e, X-ray undetected) galaxies with FIR detections, though the bulk of AGNs at any given redshift have colors that are consistent with the field population (see also the discussion of mid-IR spectra in section 8 of Nordon et al. (2012)). The most luminous AGNs typically have the warmest 24-100 colors.

The $m_{100-160}$ distributions of the AGNs and normal galaxies are more similar than their m_{24-160} distributions (also see Hatziminaoglou et al. 2010), but some small differences are noticeable. In Fig. 3 we compare the distributions of $m_{100-160}$ between AGNs and normal galaxies. At face value, we expect that the largest differences between the two sets of histograms should be at high redshift. This is because the PACS 100 and $160\mu\text{m}$

bands trace increasingly shorter rest-frame wavelengths, making the AGN emission more prominent with redshift. However, Fig. 3 shows that this is not the case. Quite surprisingly, the biggest difference between the distributions of AGNs and normal galaxies arises at low redshifts, especially in the left two panels ($z < 0.8$). The AGNs at these redshifts show a displacement to warmer FIR colors compared to the general galaxy population, with a warmer median value of the $m_{100-160}$, and lack the long tail to cooler FIR colors that is seen among normal galaxies. In the two high redshift bins, the median values of AGNs and normal galaxies are more similar, though the AGNs still show a stronger wing on the warm side of the distribution.

To quantitatively assess the level of AGN contamination in the FIR, we generate a suite of hybrid SEDs which combine AGN and SF templates picked to span the range of typical SED shapes found in real galaxies. We adopt three AGN SEDs from Mullaney et al. (2011) – a mean AGN SED, a typical high luminosity and a typical low luminosity SED² – as well as the mean QSO SED from Netzer et al. (2007), suitable for AGNs with QSO-like luminosities. For the SF templates, we consider the five basis SEDs from Mullaney et al. (2011) and add an M82-like and Arp220-like SED from the SWIRE template library

² available from <http://sites.google.com/site/decompir/>

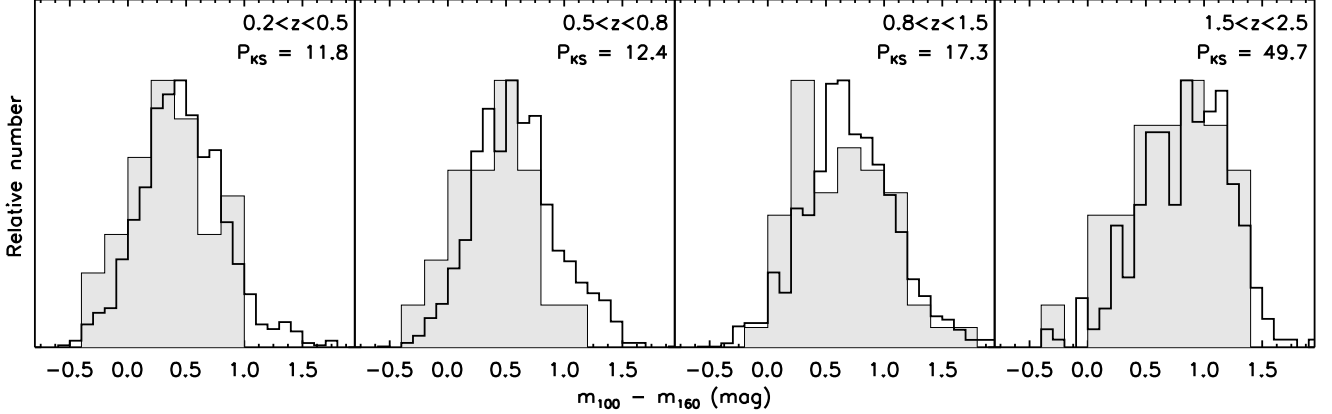


Fig. 3. Distributions of $m_{100-160}$ for COSMOS PACS-detected AGNs (shaded histogram) compared to the general population of PACS detected galaxies in the COSMOS field. Each panel is a different redshift bin, indicated in the upper right corner of the panel. Also in the upper right is a measure of the KS probability P_{KS} that the two distributions share a common parent distribution. The distributions are most different at $z < 1$ but become more similar at higher redshift. Note, systems with likely AGN contamination are not excluded from this plot.

(Polletta et al. 2007) to incorporate strongly star-bursting and ULIRG-like systems. We create AGN-dominated hybrid SEDs by adding an AGN and a SF template scaled to give a fractional contribution of AGN light $> 50\%$ at a rest-frame wavelength of $60 \mu\text{m}$.

In each panel of Fig. 2 we plot a shaded polygon that encompasses the range of observed-frame colors of these hybrid templates after they have been appropriately redshifted to the upper and lower redshift bounds of each bin. The templates that are fully AGN dominated are typically very warm in both m_{24-160} and $m_{100-160}$, and many lie outside the plots. The cooler end of the polygons are populated by hybrids with $\sim 50\%$ AGN fractions.

In all the panels, the polygons lie well away from the small black points which mark the location of the bulk of PACS detected galaxies. This is expected since most PACS detected galaxies are not likely to host an active nucleus, even those that may have obscured AGNs missed by X-ray surveys. However, it is also evident that only a few AGNs lie within these polygons at any redshift. By and large, most AGNs can safely be assumed to be dominated by cool dust emission in the FIR.

The handful of AGNs that do lie in the AGN-dominated polygons are typically quite luminous. In addition, there is a weak but general trend for the more luminous AGNs to lie closer to the polygons in all the redshift bins. This implies that some small level of AGN contamination does enter into the FIR, even around and beyond $60 \mu\text{m}$, and simply assuming that the rest-frame $60 \mu\text{m}$ luminosity in AGNs is always attributable to star-formation is probably incorrect. It is clear, however, that the vast majority of PACS detected AGNs are dominated by SF-related emission in the FIR.

Can a low level of AGN contamination in the FIR lead to the different $m_{100-160}$ distributions between AGNs and inactive galaxies? Two features of Fig. 2 suggest otherwise. Firstly, note that the shaded area of strong AGN contamination is most offset from the the locus of the data points in the lowest redshift panel and closest to the locus in the highest redshift panel. This is simply because the effects of AGN contamination on $m_{100-160}$ are least pronounced at low redshifts, for reasons already discussed. Yet, it is in these low redshift bins where the most significant differences in color distributions are seen in Fig. 3. While the ex-

clusion of AGN dominated objects does make the distributions more similar, substantial differences still remain, especially the lack of a cool wing to the AGN $m_{100-160}$ distribution. Secondly, close examination of Fig. 2 reveals that objects that make up the spread to warmer FIR colors are not always luminous AGNs, as one would expect if contamination was the reason for the spread. In addition, the part of the color-color diagram occupied by ‘warm’ AGNs at low redshifts also contains some X-ray undetected objects, implying that AGN activity is not a necessary prerequisite for having warm FIR colors. The lack of a close relationship between FIR color and AGN luminosity, coupled with an inverted trend with redshift, suggests that the offsets are not related to AGN activity, but are intrinsic to the population of galaxies that host AGNs.

In Santini et al. (2012), we show that X-ray AGNs at $z < 1$ exhibit slightly enhanced mean SFRs compared to normal galaxies of the same stellar mass, while the offset declines or disappears at higher redshifts. It is possible that the very processes that are responsible for the enhancement of mean SF activity in lower redshift AGNs may also affect their typical FIR colors. We discuss this further in §5.

We turn now to AGNs that were not detected in both PACS bands. They account for the vast majority of X-ray selected AGNs ($\approx 70\%$ in the GOODS fields, more than 90% in the COSMOS field). PACS-undetected AGNs are less star-forming, and therefore, on average, more AGN dominated at a given AGN luminosity than the PACS-detected AGNs. We can study the FIR properties of PACS-undetected AGNs only through their mean stacked signal. In the lower panels of Fig. 2, we compare the mean colors of the PACS undetected AGNs to the PACS detected AGNs. The stacked points come from individual measurements in all three fields, while the black points here are only from the COSMOS dataset and serve only to place the stacked points in context. The stacks were restricted to objects that were detected in the $24 \mu\text{m}$ band, in order to allow an accurate estimate of the mean $24 \mu\text{m}$ flux. As before, we include the polygons that delineate regions in the diagrams occupied by AGN-dominated SEDs at $60 \mu\text{m}$ rest.

By and large, the colors of the PACS stacked AGNs lie outside the shaded polygons, implying that the stacked signal is not dominated at $60 \mu\text{m}$ by AGN light. However, as expected

they tend to lie closer to the polygons than the bulk of detected AGNs, clustering around the right edges where templates with AGN fractions of a few tens of percent would lie. Some or most of the stacks in any given redshift bin lie within the region of AGN dominance. In general, the scatter of stacked points lies closer to the polygons in the higher redshift bins, as expected if the shift to warmer colors is a result of AGN contamination.

In addition, the stacks of the more luminous AGNs (redder points) have consistently warmer colors. Most of the variation with AGN luminosity happens through the m_{24-160} color. Systematic changes in $m_{100-160}$ are not clearly discernable and the typical FIR colors of the stacked AGNs are consistent with the typical colors of the detected AGNs. This highlights the fact that FIR colors are not greatly affected by increases in AGN luminosity, unlike the accretion sensitive MIR SED. We conclude that, at lower redshifts ($z < 1$) AGN contamination in the FIR is minor in both PACS detected and stacked samples and very rarely gets above 50%. However, at higher redshifts out to $z = 2.5$, the AGN can substantially affect $m_{100-160}$ and, therefore, our estimate of the rest-frame 60 μm luminosity.

4. Results

Using measurements of L_{60} , the mean rest-frame 60 μm luminosity from all 3 fields combined (Appendix B), we will now study the relationship between FIR emission and SMBH accretion to $z = 2.5$. We first look at mean trends that come from combining fluxes from detections and stacks in the PACS bands to get a single mean value for L_{60} in each bin in redshift and X-ray luminosity. In the following sections, we extrapolate L_X to a bolometric AGN luminosity (L_{AGN}) using the following relation, which is based on Eqn. 5 from Maiolino et al. (2007) and taking a ratio of 7 between the luminosity at 5100Å and L_{AGN} (Netzer & Trakhtenbrot 2007).

$$\log L_{AGN} = \frac{(\log L_X - 11.78)}{0.721} + 0.845 \quad (1)$$

where L_X (the 2-10 keV band X-ray luminosity) and L_{AGN} are in erg s^{-1} .

4.1. Mean trends: L_{60} against L_{AGN}

In Fig. 4, L_{60} is plotted against L_{AGN} . The plotted L_{AGN} is the median value for objects in all three fields in AGN luminosity bin, while error bars in L_{AGN} show the interpercentile range in AGN luminosity containing 80% of the sample – typical errors in AGN luminosity are smaller than the error bars shown here. Different colors are used to represent measurements in the different redshift intervals. All the mean measurements from the Herschel fields have been tabulated in Table 1. In the plot, we include as well data for the local sample of Swift BAT AGNs (black points and line). Included as well in the figure is the relation from Netzer (2009) (dashed line) and colored solid curves which come from our fits in §4.1.1. This plot may be compared directly to Fig. 6 of Shao et al. (2010) and is analogous to Fig. 5 in Mullaney et al. (2012).

We also include a shaded zone which shows the range in the plot occupied by pure AGNs (no star-formation) with the SEDs described in §3.1. These SEDs are expected to span the majority of true AGN SED shapes in nature. The tight correlations between L_X and 12.3 μm IR luminosity among local AGNs (Gandhi et al. 2009) are used to link the bolometric AGN luminosity (derived from L_X) and the FIR luminosity (through the

AGN IR SEDs). While, at low AGN luminosities, torus emission will not contribute measurably to the mean FIR luminosity, it plays an increasingly greater role at high AGN luminosities. Indeed, quite surprisingly, our L_{60} measurements for the most luminous AGNs at $z > 1$ are consistent with their mean SEDs having low or no star-formation. On the other hand, the average of AGN+host SEDs should be above the pure AGN SED if even some objects have star formation. This may indicate that our adopted intrinsic AGN SEDs are too FIR-bright, as suggested by Mor & Netzer (2012).

At redshifts below $z = 0.8$, the variation of L_{60} with L_{AGN} shows a consistent behavior. At low AGN luminosities, L_{60} is weakly correlated or uncorrelated with AGN luminosity, and approximately constant over two orders of magnitude in L_{AGN} . This constant FIR luminosity, which we call L_{60}^b , is redshift dependent and rises by a factor of ≈ 3 between $z = 0$ and $z = 0.65$ (the mean redshift of galaxies in the $0.5 < z < 0.8$ bin).

At higher AGN luminosities, a change is seen. Beyond a certain transition in L_{AGN} , L_{60} begins to correlate strongly with L_{AGN} . This is most evident in the local BAT sample and among AGNs in the $0.5 < z < 0.8$ bins, which both span a sufficiently large range in L_{AGN} to bring out this trend. The slope of the correlation is comparable in both redshift bins. The transition AGN luminosity, which we call L_{AGN}^c , increases with redshift, by about an order of magnitude between $z = 0$ and $z = 0.8$.

While lower redshift AGNs show a particular relationship between L_{60} and L_{AGN} , the situation appears to change at higher redshifts ($z > 0.8$). The correlation between L_{60} and L_{AGN} is weak or absent. The overall trend is much flatter than for AGNs at lower redshifts, implying that beyond $z \sim 1$ the FIR emission of the AGN hosts is quite independent of the accretion luminosity of the nucleus. L_{AGN}^c is not well characterised at these redshifts.

Having said this, we note that these inferences come primarily from measurements of the highest luminosity AGNs in our sample, which are significantly lower than expected from an extrapolation of the low redshift correlation. This measurement in the $0.8 < z < 1.5$ redshift bin is rather uncertain since it depends on a combination of only four objects and is subject to large statistical uncertainties. The measurement in the $1.5 < z < 2.5$ bin is more robust. We have individually examined the optical and IR images of these luminous AGNs, as well as the X-ray spectral fits, to ensure that they are not affected by incorrect multi-wavelength associations or large errors. Therefore, we believe that the flattening of the L_{60} - L_{AGN} relationship among luminous AGNs at high redshifts is a real effect.

The increase in the mean L_{60} of low luminosity AGNs continues to $z = 2.5$. The change in L_{60}^b accelerates between $z \sim 1$ and $z \sim 2$, to reach $L_{60}^b \sim 10^{45} \text{ erg s}^{-1}$ at $1.5 < z < 2.5$. This is somewhat at odds with the increase in the star-formation density of field galaxies with redshift, which typically rises sharply to $z \approx 1$ and flattens out towards higher redshift (Hopkins & Beacom 2006). However, AGN are typically hosted by massive galaxies (Brusa et al. 2009; Xue et al. 2010; Rosario et al. 2011) which have star-formation histories that are different from the bulk of star-forming galaxies at these redshifts (Pérez-González et al. 2008). Star-formation ‘downsizing’ requires that such massive galaxies go through most of their star-formation around or earlier than $z \sim 2$ and contribute less to the integrated FIR luminosity density of the Universe at $z < 1$ than at higher redshifts. Therefore, we would expect AGN hosts to have a higher rate of increase of L_{60}^b at $1 < z < 2$ than at $z < 1$ (Santini et al. 2012).

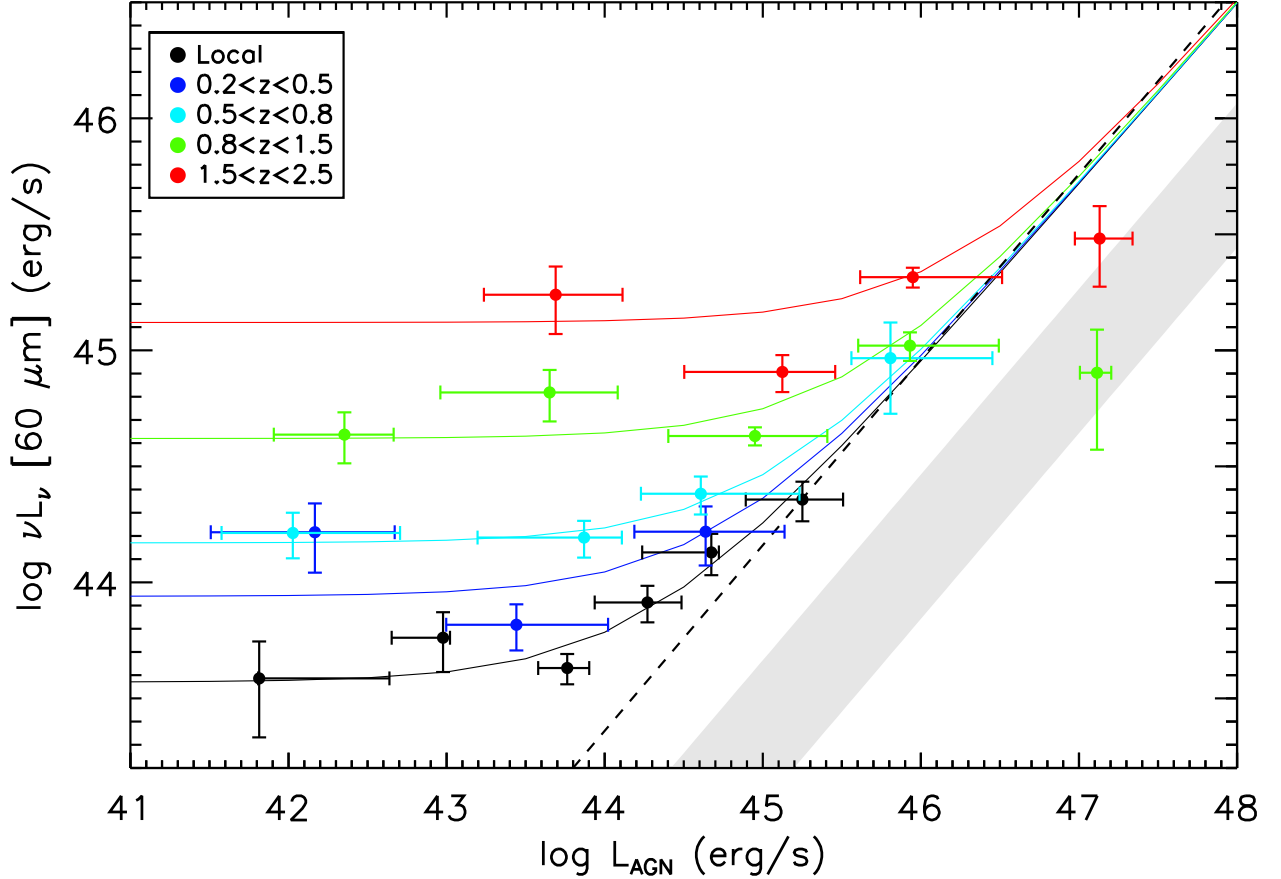


Fig. 4. Mean $\nu L_\nu(60\mu\text{m})$ (L_{60}) vs. L_{AGN} of X-ray selected AGNs in 5 different redshift bins from the local Universe to $z = 2.5$. The colored data points are combinations of mean measurements in 3 PEP fields: GOODS-N/S and COSMOS, while the black data points come from our analysis of the SWIFT BAT sample. The solid colored lines are functional fits to the mean measurements, as described in §4.1.1. The dashed line is the correlation line shown by AGN-dominated systems in Netzer (2009). The shaded region corresponds to the approximate 1σ range exhibited by empirical pure-AGN SEDs. At low redshifts, a strong change in the mean trend exists as a function of L_{AGN} , which disappears at high redshifts. The mean L_{60} of low-luminosity X-ray AGNs increases monotonically with redshift, mirroring the increase in the mean SFR of massive galaxies across redshift.

4.1.1. Fits to the $L_{60} - L_{AGN}$ trend

We model the trend between $\log L_{60}$ and $\log L_{AGN}$ in each of the five redshift bins as a combination of a flat line (a constant value L_{60}^b) and a straight line with a positive non-zero slope α . The constant value is determined by the mean SFR of low-luminosity AGN hosts and is unrelated to accretion activity. We capture the correlation between $\log L_{AGN}$ and $\log L_{60}$ as a linear relationship, essentially a regression line. In total, three parameters define the fit: L_{60}^b , α and the intercept of the regression line. The intercept also defines L_{AGN}^c , which we take to be the value of L_{AGN} where the regression line ordinate = L_{60}^b , i.e., the AGN luminosity where SF activity that is correlated with BH growth starts to dominate the total SFR of the host galaxy.

We fit the measured data using a non-linear least-squares fitting procedure (CURVEFIT in IDL). Results are tabulated in Table 2. In the two lower redshift bins where a good fit is possible (local and $0.5 < z < 0.8$) we arrive at consistent values for the slope of the regression line ($\alpha \approx 0.75 \pm 0.23$). L_{60}^b increases strongly with redshift, as expected.

Among the two higher redshift bins, the transition is not well-defined. A best-fit slope of the regression line is lower ($\alpha \sim 0.5 \pm 0.23$) and L_{AGN}^c is about 1.5 dex higher than at lower redshifts. However, the quality of the fit is rather poor (reduced $\chi^2 \gtrsim 3.5$) in both these redshift bins and, in fact, a single straight line with a variable slope fits the data points just as well.

A correlation between AGN luminosity (or mass accretion rate) and host galaxy SF rate has been reported by several studies, for local low-luminosity Seyferts (Netzer 2009; Diamond-Stanic & Rieke 2011) and high redshift AGNs and QSOs (Lutz et al. 2008; Hatziminaoglou et al. 2010; Bonfield et al. 2011). Netzer (2009) compared the SFRs of local SDSS Type II and LINER AGNs and find that they lie on the same relationship as luminous PG QSOs (Netzer et al. 2007) and the mm-bright QSOs at $z \sim 2$ (Lutz et al. 2008). The slope of this relationship is approximately 0.8, quite consistent with our own estimate of α . The relationship in Netzer (2009) extends linearly to low values of AGN luminosity ($L_{AGN} < 10^{43}$ erg s $^{-1}$), while we find a very definite turnover to a flat relationship below L_{AGN}^c , most likely since Netzer (2009) specifically concentrated on AGN-dominated galaxies.

Table 1. Mean Rest-frame 60 μm luminosities in bins of Redshift and Hard-band X-ray Luminosity.

Redshift bins	Bins in De-absorbed 2-10 keV band X-ray luminosity L_X				
COSMOS	41 – 42	42 – 43	43 – 44	44 – 45	45 – 45.5
0.2 – 0.5	43.17 – 44.04 (18)	43.72 – 43.93 (100)	44.07 – 44.33 (34)	— (2)	— (0)
0.5 – 0.8	— (1)	44.03 – 44.24 (73)	44.19 – 44.42 (123)	44.73 – 45.12 (13)	— (0)
0.8 – 1.5	— (0)	44.39 – 44.96 (28)	44.59 – 44.68 (434)	44.97 – 45.11 (134)	44.57 – 45.09 (4)
1.5 – 2.5	— (0)	— (0)	44.78 – 44.98 (152)	45.30 – 45.39 (295)	45.27 – 45.62 (23)
GOODS-S	41 – 42	42 – 43	43 – 44	44 – 45	45 – 45.5
0.2 – 0.5	44.02 – 44.49 (11)	— (1)	— (1)	— (0)	— (0)
0.5 – 0.8	43.90 – 44.14 (30)	44.04 – 44.45 (19)	43.94 – 44.35 (11)	— (1)	— (0)
0.8 – 1.5	43.99 – 44.61 (18)	44.40 – 44.93 (27)	44.43 – 44.75 (23)	44.88 – 45.15 (3)	— (0)
1.5 – 2.5	— (3)	45.02 – 45.39 (20)	44.66 – 45.05 (32)	44.87 – 45.13 (5)	— (0)
GOODS-N	41 – 42	42 – 43	43 – 44	44 – 45	45 – 45.5
0.2 – 0.5	43.88 – 44.41 (12)	42.95 – 43.81 (5)	— (2)	— (0)	— (0)
0.5 – 0.8	44.23 – 44.59 (22)	44.03 – 44.34 (10)	44.36 – 44.67 (5)	— (0)	— (0)
0.8 – 1.5	44.53 – 44.77 (33)	44.69 – 44.98 (47)	44.51 – 44.71 (39)	44.28 – 44.75 (6)	— (0)
1.5 – 2.5	— (3)	44.89 – 45.42 (16)	44.72 – 45.11 (44)	44.08 – 45.27 (5)	— (0)

Notes. Mean Rest-frame 60 μm luminosities are in units of $\log \text{erg s}^{-1}$. Numbers in parentheses indicate the number of galaxies that contribute to the mean measurement in each redshift and X-ray luminosity bin.

Table 2. Functional fits to the Trends between L_{60} and L_{AGN} in bins of Redshift

Slope of Regression Line α left free					
Redshift bins	L_{60}^b ¹	α ²	L_{AGN}^c ³	$\bar{\chi}^2$	$\bar{\chi}^2$ (single line fit) ⁴
Local	43.56 ± 0.12	0.75 ± 0.22	44.23 ± 0.13	1.53	N/A
0.5 – 0.8	44.18 ± 0.08	0.84 ± 0.30	44.94 ± 0.33	0.41	N/A
0.8 – 1.5	44.60 ± 0.09	0.58 ± 0.18	45.99 ± 0.64	7.58	7.65
1.5 – 2.5	45.08 ± 0.08	0.53 ± 0.25	46.46 ± 0.82	7.57	6.97
Slope of Regression Line α fixed at 0.78					
Redshift bins	L_{60}^b	α	L_{AGN}^c	$\bar{\chi}^2$	
Local	43.57 ± 0.08	0.78	44.27 ± 0.11	1.14	—
0.2 – 0.5	43.94 ± 0.09	0.78	44.82 ± 0.41	6.47	—
0.5 – 0.8	44.17 ± 0.07	0.78	44.89 ± 0.22	2.42	—
0.8 – 1.5	44.62 ± 0.04	0.78	45.98 ± 0.17	5.61	—
1.5 – 2.5	45.12 ± 0.06	0.78	46.51 ± 0.21	5.39	—

Notes. See §4.1.1. ⁽¹⁾ Mean L_{60} of low-luminosity AGNs ⁽²⁾ Slope of Regression line valid for luminous AGNs ⁽³⁾ Transition AGN luminosity: L_{60} is significantly correlated with L_{AGN} at $z < 1$ beyond this AGN luminosity ⁽⁴⁾ A single straight line fit between $\log L_{AGN}$ and $\log L_{60}$ with a variable slope and normalisation.

If we assume that the slope of the regression line is constant across redshift, as suggested by Netzer (2009), then the fits to our lower redshift data points gives the following relation:

$$\log \frac{L_{60}}{10^{44} \text{erg s}^{-1}} = \log \left(\frac{L_{AGN}}{6.3 \times 10^{44} \text{erg s}^{-1}} \right)^{0.78} \quad (2)$$

We rerun our fits now fixing the regression line to Eqn. 2 and derive a second, more refined set of values for L_{60}^b , which are also listed in Table 2. In Fig. 4, we include lines which show the *expected* trends in each of our five redshift intervals as solid colored lines. The data points for AGNs in the three lower redshift bins follow the trends quite well, since the trends were calibrated on these points. At high redshifts, the high L_{AGN} measurements lie systematically off the expected trend, by as much as 3-4 σ for AGNs at $z \sim 1$ and by around 2 σ at $z > 1.5$. L_{60} for these highest luminosity AGNs appear to be comparable to, or perhaps slightly higher than, L_{60}^b at their corresponding redshifts. In other words, the mean FIR luminosity of the brightest AGNs at $z \gtrsim 1$ are not very different from those of low-luminosity AGNs or normal massive galaxies at these redshifts. This may be contrasted with the rather drastic change in the L_{60} with L_{AGN} among AGNs at lower redshifts. This suggests that there is a change in

the relationship between SF and AGN activity between luminous AGNs at low and high redshifts, which becomes important around $z \sim 1$.

4.2. Distributions of L_{60} against L_{AGN}

Till now, we have concentrated on the mean FIR properties of the AGN population. Underlying these mean measurements is a distribution of FIR luminosities which can have considerable intrinsic scatter. We turn now to an examination of the L_{60} distribution by considering separately properties of AGNs both detected and undetected in the PACS imaging.

In Fig. 5, we plot $\nu L_{\nu}(60\mu\text{m})$ against L_{AGN} for PACS-detected AGNs on a diagram similar to that used for the mean measurements in Fig. 4. We also indicate the location in this diagram of the stacked measurements for PACS undetected AGNs using colored numbers which list the number of objects that go into a given stack. Since the X-ray and PACS depths of the COSMOS field is considerably lower than the GOODS fields, we make separate panels in the Figure for COSMOS and the combined GOODS fields.

If we concentrate first on PACS detected AGNs, a clear correlation can be seen between AGN luminosity and $\nu L_{\nu}(60\mu\text{m})$ in

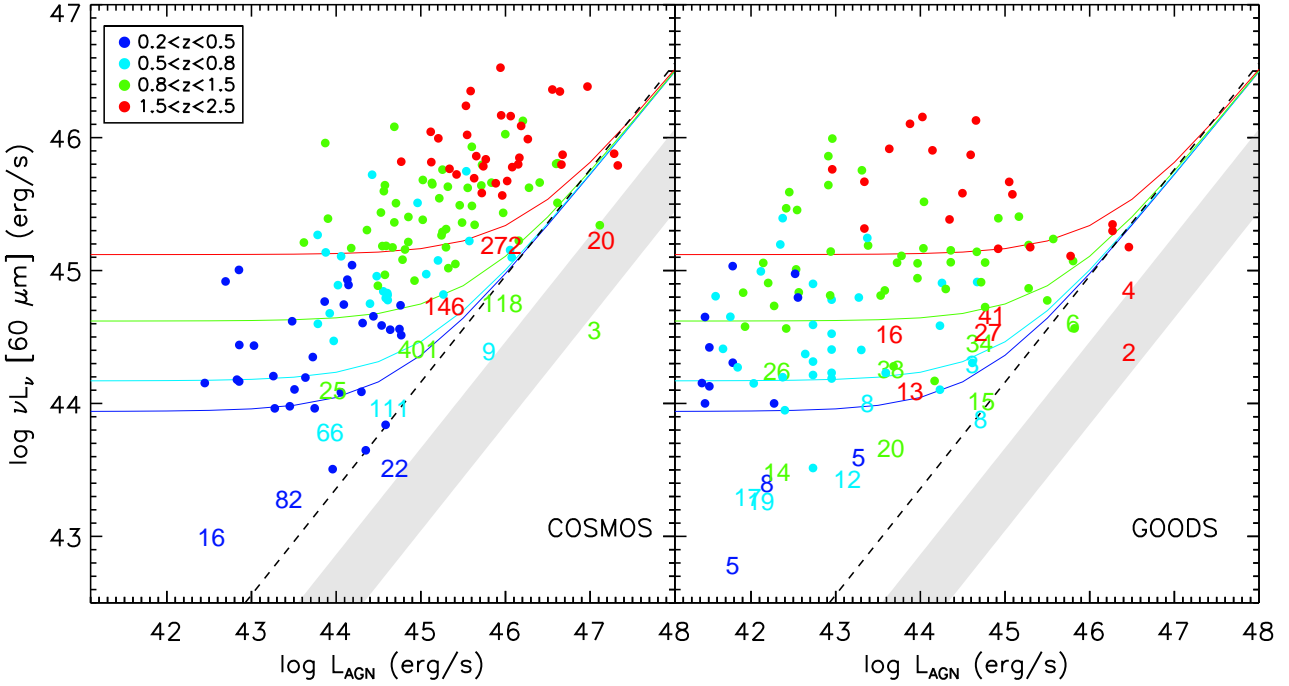


Fig. 5. $\nu L_{\nu}(60\mu\text{m})$ vs. L_{AGN} of X-ray selected AGNs in 4 redshift bins from $z = 0.2$ to $z = 2.5$. Galaxies in the GOODS and COSMOS fields have been separated into right and left panels respectively, as they differ greatly in both X-ray and PACS depths. Colored points are AGNs detected in both bands. Colored numbers show the location of stacked measurements and the number of objects that go into the stack. Dashed and solid lines, as well as shaded regions, are the same as in Fig. 4. Note the apparent correlation in the colored points in the left panel, which is absent in the right panel. The correlation is primarily driven by selection effects inherent with wide and shallow surveys.

the COSMOS dataset if we consider AGNs at all redshifts together. While this correlation has a slope that matches that of the regression line that we derive above for high-luminosity AGNs, it is offset from the line by approximately an order of magnitude in $\nu L_{\nu}(60\mu\text{m})$. The correlation disappears, however, when one considers PACS detected AGNs in the GOODS fields, even though there is a large degree of overlap in L_{AGN} between the two samples. The correlation among COSMOS AGN is not real – it is driven primarily by strong selection effects in the AGN sample with redshift. At high redshifts, the rare X-ray and FIR luminous AGNs which are not found in low redshift bins due to smaller survey volumes start to be represented significantly in the COSMOS sample. This effect can be seen even within a single large redshift bin (for e.g., the green points at $0.8 < z < 1.5$) though the apparent correlation is weaker. The much smaller survey volume of the combined GOODS fields ensures that luminous AGNs are under-represented at all redshifts allowing for a more uniform AGN sample, which weakens the aforementioned selection effects and, by extension, the apparent correlation between $\nu L_{\nu}(60\mu\text{m})$ and L_{AGN} . We suggest that relationships between star-formation and nuclear activity in AGNs in the literature that are based on individual detections from shallow, large-area surveys may be strongly affected by such selection effects (e.g., Hatziminaoglou et al. 2010).

In general, the stacked measurements are up to an order of magnitude less luminous than the weakest PACS-detected sources (see also Fig. B.1). A substantial fraction of AGNs, especially at lower redshifts, are hosted by quenched galaxies (Santini et al. 2012). Since star-formation is very weak to negligible in such hosts, they are expected to lie well below the PACS detection limit at all redshifts and therefore contribute only to the stacked measurements.

4.3. Mean trends: N_H against L_{AGN}

We turn now to the variation of L_{60} with X-ray obscuration, parameterised by the column density of absorbing hydrogen N_H . The major merger model for AGN fueling and evolution predicts that most BH growth occurs when the AGN is enshrouded by a dense dusty obscuring envelope at the center of a merger remnant (e.g., Sanders et al. 1988). If mergers are responsible for fueling most of the X-ray AGN population, as some evolutionary models propose (e.g., Somerville et al. 2008), there should be definite trends between the obscuration of AGNs and their mean SFR.

We explore this in Fig. 6, where we plot L_{60} against N_H in the four redshift bins that we used in earlier figures. To ensure a clean AGN sample, only sources with $L_X > 10^{42}$ erg s $^{-1}$ were used to make this plot. At each redshift bin, we split the AGNs into six bins in obscuration: $\log N_H$ (cm $^{-2}$) of < 20.5 , 20.5-21, 21-22, 22-23, 23-24, > 24 . The plotted value of N_H for each data point is the median value for all AGNs in that bin and the error bars show the interpercentile range containing 80% of the sample. Measurements from all three fields have been combined in this Figure.

In general, the trend between L_{60} and N_H is weak. At $0.5 < z < 0.8$, L_{60} appears to increase slowly with N_H by about 0.4 dex across 3 orders of magnitude in the obscuring column, though unobscured AGNs also show a higher mean L_{60} . The measurement for the intermediate bin in N_H is consistent with the L_{60}^b of the AGN population at this redshift, while bins with higher obscuration are slightly enhanced compared to this value. This trend appears to be driven more by selection effects in L_X - N_H space than by true correlations between L_{60} and N_H (see Fig. 1 and associated discussion) and is not particularly significant. At

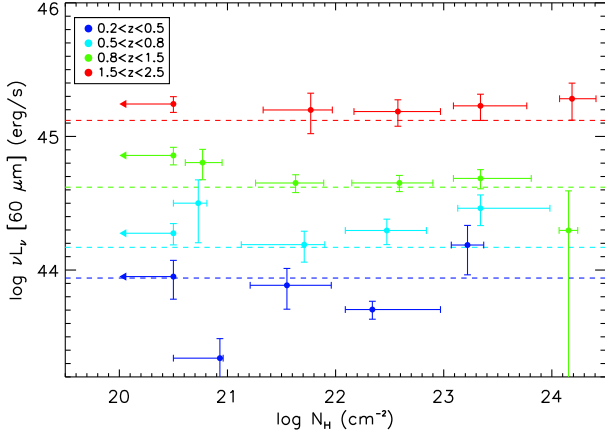


Fig. 6. L_{60} vs. N_H in 4 different redshift bins in the redshift range $0.2 < z < 2.5$. The dashed lines show L_{60}^b in each redshift bin, taken from Fig. 4. All objects with N_H consistent with Galactic absorption contribute to the point at $N_H \leq 10^{20.5} \text{ cm}^{-2}$, irrespective of the different Galactic absorption towards the three different fields. L_{60} is relatively flat across a large range in N_H with no clearly discernible trends, especially among well-measured points. As discussed in §4.3, covariances between L_X and N_H , driven by selection effects in the population of obscured AGNs, can affect trends in this figure, but the general results shown here should be relatively robust, since we combine measurements from fields of very different X-ray depths.

$0.8 < z < 1.5$ and $1.5 < z < 2.5$, the increase of L_{60} with N_H is weaker, consistent with a flat trend.

At every redshift, a subset of AGNs have $N_H < 10^{20.5} \text{ cm}^{-2}$, consistent with a very low or pure Galactic obscuration. In general, L_{60} for these objects is comparable to or higher than those of more obscured AGNs.

We note here our AGN sample differs considerably from the luminous QSO samples for which a link between X-ray obscuration and SFR has been previously been suggested (Page et al. 2001, 2004; Stevens et al. 2005). The bulk of our AGNs are typically below the knee of the X-ray LF, while those studies concentrated on special populations of X-ray absorbed optical broad-line QSOs. In addition, the typical AGN luminosity of our X-ray sample increases with redshift (Fig. 1). At $z < 1$, most AGNs that contribute to Fig. 6 are of low and moderate luminosity, while at $z > 1$, they are increasingly luminous AGNs where merger-driven processes may be expected to be most relevant.

Another simple, model-independent way to broadly separate obscured and unobscured AGNs is through their Hardness Ratio (HR), defined as $HR = (H - S)/(H + S)$ where H are the photon counts in the hard band (2-10 keV) and S are the photon counts in the soft band (0.5-2 keV). If the typical SFRs of obscured AGNs were significantly enhanced, as suggested by models of AGN fueling by gas-rich major mergers, then we expect them to be more frequently detected by PACS (or other FIR surveys) compared to unobscured AGNs (e.g., Page 2011).

In Fig. 7, we plot HR against redshift for AGNs in the GOODS-S field. Despite the lower number statistics, we use this field for this plot because the PACS data is the deepest here and the detection fractions are not swayed by the statistics of the most FIR luminous systems, typically strong starbursts. The PACS detection fractions, estimated using Bayesian binomial statistics (Cameron 2011), of AGNs above and below

our fiducial boundary between unobscured and obscured AGNs (solid curve: $N_H = 10^{22} \text{ cm}^{-2}$) are comparable in all four of our redshift bins. Similar results are found in the GOODS-N and COSMOS fields: any differences in the detection fractions between obscured and unobscured AGNs are at a 1σ level and not significant, given the typical uncertainties in X-ray counts.

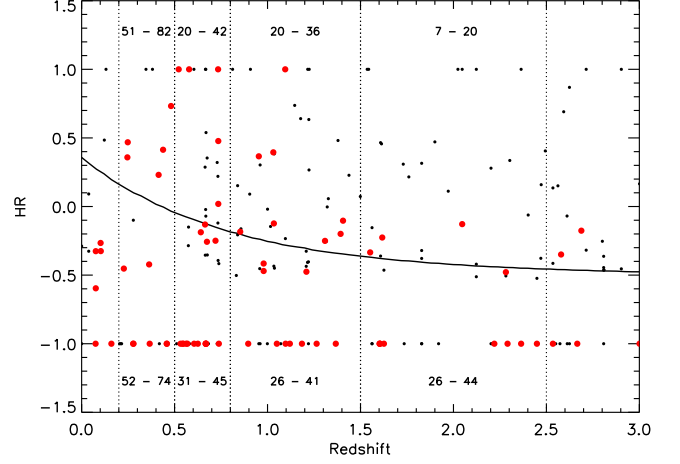


Fig. 7. The observed hardness ratio (HR) of GOODS-S X-ray AGNs as a function of redshift. Large red points show PACS detected AGNs and small black points are PACS-undetected AGNs. Objects detected only in the hard(soft) bands have $HR = 1$ and $HR = -1$ respectively. The solid black line shows the expected HR for a power-law X-ray spectrum with a typical photon index of $\Gamma = 1.9$ and an obscuring Hydrogen column density of $N_H = 10^{22} \text{ cm}^{-2}$. Dotted vertical lines mark the 4 redshift bins used in this study. The numbers in each bin give the 1σ range in PACS detection fraction (in %) for obscured X-ray AGNs (i.e., those above the solid line – upper set of numbers) and unobscured X-ray AGNs (i.e., those below the solid line – lower set of numbers). A quick examination will reveal that PACS detection fractions of obscured and unobscured AGNs are similar, with only insignificant differences in any given redshift bin.

5. Discussion

Using deep X-ray catalogs and high-quality FIR imaging from Herschel/PACS, we have estimated the mean FIR luminosities of AGNs across a wide span in redshift and SMBH accretion luminosity. We have studied the variation of the 60 μm specific luminosity with L_{AGN} and find that L_{60} is independent of L_{AGN} at low accretion luminosities, but can show a strong correlation with L_{AGN} at high accretion luminosities. The strength of the correlation depends on redshift – while strong at low redshifts ($z < 0.8$), the correlation appears to weaken or disappear at high redshifts. In this section, we discuss the implications of our results on our knowledge of the process of AGN fueling, its evolution with redshift and its dependence on the nature of the host galaxy.

The rest-frame FIR is widely regarded as the preferred tracer of star-formation in galaxies since it is particularly sensitive to cool dust emission which dominates the output of star-forming regions. However, as we show in §3, the tail of FIR emission from hot dust heated by an active nucleus can influence the FIR

Table 3. Mean Rest-frame $60\ \mu\text{m}$ luminosities in bins of Redshift and X-ray Obscuring Column.

Redshift bins	Bins in Column Density of Obscuring Hydrogen N_H ($\log\ \text{cm}^{-2}$)					
	19 – 20.5	20.5 – 21	21 – 22	22 – 23	23 – 24	24 – 25
COSMOS						
0.2 – 0.5	43.78 – 44.07 (45)	43.12 – 43.49 (4)	43.71 – 44.01 (36)	43.90 – 44.17 (46)	43.96 – 44.33 (4)	— (0)
0.5 – 0.8	44.20 – 44.45 (77)	44.20 – 44.68 (5)	44.06 – 44.31 (38)	44.02 – 44.37 (76)	44.61 – 45.08 (13)	— (0)
0.8 – 1.5	44.74 – 44.89 (248)	44.86 – 45.22 (13)	44.58 – 44.72 (88)	44.61 – 44.76 (212)	44.71 – 45.00 (37)	— (2)
1.5 – 2.5	45.18 – 45.31 (289)	— (2)	45.02 – 45.33 (35)	45.09 – 45.31 (84)	45.16 – 45.41 (58)	45.13 – 45.49 (3)
GOODS-S						
0.2 – 0.5	— (0)	— (0)	— (0)	— (0)	— (1)	— (0)
0.5 – 0.8	43.68 – 44.69 (7)	— (2)	43.59 – 44.33 (3)	43.87 – 44.31 (11)	43.80 – 44.07 (7)	— (1)
0.8 – 1.5	44.49 – 45.33 (8)	— (2)	43.96 – 44.47 (8)	44.38 – 44.83 (19)	44.18 – 44.72 (14)	— (2)
1.5 – 2.5	44.82 – 45.40 (8)	— (0)	<44.59 (6)	43.88 – 44.78 (17)	44.54 – 45.23 (23)	<44.60 (3)
GOODS-N						
0.2 – 0.5	— (2)	— (0)	— (1)	43.39 – 43.54 (3)	— (0)	— (1)
0.5 – 0.8	44.06 – 44.29 (3)	— (1)	— (2)	44.22 – 44.51 (5)	— (2)	— (2)
0.8 – 1.5	44.74 – 45.12 (19)	44.13 – 44.44 (3)	44.04 – 45.29 (11)	44.40 – 44.64 (22)	44.51 – 44.68 (30)	42.66 – 44.59 (7)
1.5 – 2.5	< 45.04 (11)	— (1)	< 45.44 (4)	44.73 – 45.44 (14)	44.82 – 45.23 (27)	44.86 – 45.36 (8)

Notes. Mean Rest-frame $60\ \mu\text{m}$ luminosities are in units of $\log\ \text{erg}\ \text{s}^{-1}$. Numbers in parentheses indicate the number of galaxies that contribute to the mean measurement in each redshift and N_H bin.

emission in AGN host galaxies, and in some cases, may dominate the $60\ \mu\text{m}$ luminosity of such systems. While the likelihood of AGN dominance in the FIR depends positively on the luminosity of the AGN, this is by no means a simple one-to-one relationship. Galaxies that are luminous in the FIR (PACS detected AGNs) are usually SF-dominated with a small fraction that are AGN-dominated. FIR weak galaxies (undetected in the PACS imaging) are, on average, SF-dominated as well.

5.1. Two regimes of AGN-galaxy co-evolution?

Our results show that, among $z < 1$ galaxies with relatively luminous AGNs ($L_{\text{AGN}} \gtrsim 10^{44}\ \text{erg}\ \text{s}^{-1}$), the mean nuclear activity closely tracks the bulk of star-formation. At lower AGN luminosities, on the other hand, star-formation is unrelated to AGN luminosity. This suggests two regimes in the relationship between global star-formation in AGN hosts and nuclear activity.

The first regime, applicable to low luminosity AGNs, requires a disconnect between instantaneous AGN accretion and host star-formation across the galaxy. The processes that drive and regulate most of the star formation in such host galaxies do not directly fuel the SMBH. The second regime, applicable to high luminosity AGNs, is one in which the SMBH accretion tracks the total SFR of the host galaxy. Here we expect direct coordination between global SF processes and the fueling of the AGN, over timescales that are short compared to the duty cycle of AGN activity ($\sim 10^{7-8}\ \text{yr}$, Martini & Weinberg 2001; Hopkins et al. 2005).

One of the best candidates for a process that directly links global SF and SMBH accretion are galaxy mergers, signatures of which are relatively common among local AGNs (Koss et al. 2010). Morphological studies of low-redshift star-forming QSOs also find frequent merger signatures (Canalizo & Stockton 2001; Urrutia et al. 2008; Veilleux et al. 2009). QSO hosts frequently show bluer colors than typical old red ellipticals, in support of their recent merger origin (Jahnke et al. 2004). However, a substantial fraction of QSO hosts show characteristics of undisturbed disks, inconsistent with a pure merger origin for all QSOs (Bahcall et al. 1997; Dunlop et al. 2003; Guyon et al. 2006). The question of whether the most luminous AGNs are always associated with mergers is still somewhat open. Part of the reason for this uncertainty is that the structural identification of bona-

fide mergers is not entirely straightforward (Lotz et al. 2011, and references therein). Studies of moderate luminosity X-ray AGNs find no excess of merger signatures compared to inactive galaxies (e.g. Grogin et al. 2005), and only weak trends with AGN luminosity (Cisternas et al. 2011; Kocevski et al. 2012). However, these studies are usually limited to AGN luminosities below L_{AGN}^c , with very limited statistics at higher luminosities. In addition, our results seem to suggest that the role of mergers as drivers of luminous AGNs may diminish at high redshifts, exactly where such studies have concentrated.

5.2. The connection between SFR and L_{AGN} in recent merger simulations

It is instructive to test if the correlation observed among AGNs at $z \lesssim 1$, which we attribute to galaxy mergers, is indeed in agreement with models that trace the evolution of both star formation rate and accretion onto the black hole during a galaxy merger.

We have approached this by re-visualizing results from a set of current merger models. We use the models studied by Wuyts et al. (2010) which focus on progenitor galaxies with size and high gas content as expected for $z \sim 2$ mergers, as well as a fully analogous set of models which encompass the larger sizes and lower gas content of local mergers (Cox et al. 2006). In brief, all these models use the Gadget-2 smoothed particle hydrodynamic code (Springel 2005) and prescriptions for star formation, supernova feedback, black hole growth and AGN feedback to trace the evolution of merging galaxies. For more details, we refer the reader to Wuyts et al. (2010) and references therein. At $z \sim 2$, 25 simulations cover a number of interaction geometries of compact high- z disks with gas fractions around 80%, while at $z \sim 0$ 30 simulations span different geometries for gas fractions 5–20%.

We caution that this suite of models samples only a small part of the possible parameter space of progenitor properties and interaction geometries, and that the treatment of star formation and accretion is approximate – the accretion rate follows the Bondi mechanism for the circumnuclear conditions at the model’s spatial resolution of order 100 pc. However, these models represent among the best attempts at this time to integrate SMBH accretion into galaxy mergers and can certainly allow a feasibility test of

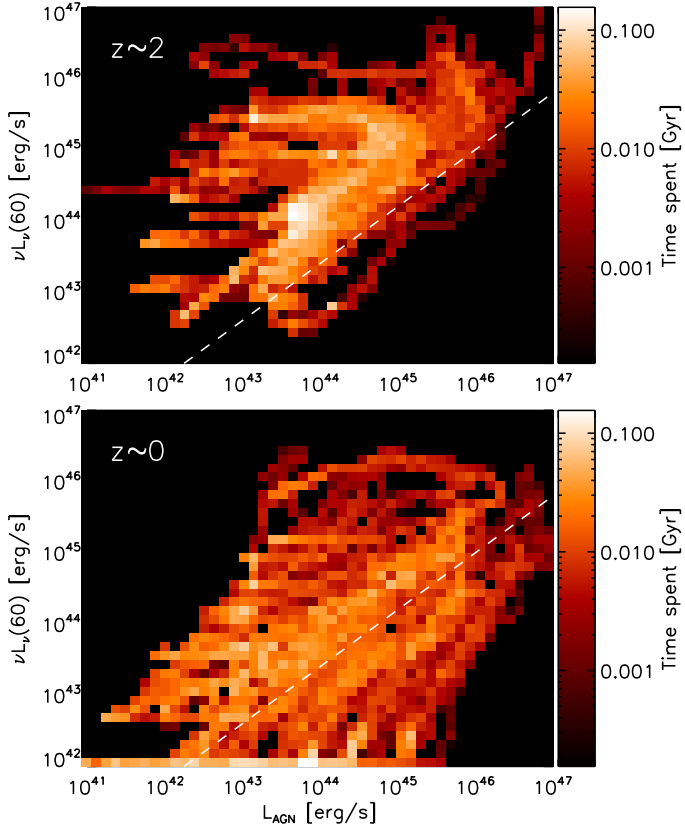


Fig. 8. Average time spent by hydrodynamic merger models (see text) in different regions of the plane defined by AGN luminosity and star forming luminosity. Top: $z \sim 2$ mergers of gas rich progenitors. Bottom: local mergers. The dashed line indicates the relation $\nu L_{\nu}(60\mu\text{m}) \propto L_{\text{AGN}}^{0.8}$ of Netzer et al. (2009).

whether mergers produce an overall correlation between galaxy-wide SFR and L_{AGN} .

The two panels of Fig. 8 visualize the time that the mergers spend in different regions of the SFR/ L_{AGN} plane. These figures include tracks from all merger models together, separated only by their redshift regime. Any individual merger model generally takes a rather complicated path in the SFR/ L_{AGN} plane, suggesting that there is strictly no real tight synchronisation between the two processes. However, when taking the suite of models as a whole, it is clear that much time is indeed spent near the ‘correlation line’ from Netzer (2009) and §4.1, mostly when star formation and accretion decay after the merger. Such behavior is seen among mergers appropriate for both low and high redshift progenitors.

We refrain from making further detailed conclusions due to the limitations of this approach and since the scope of this discussion is limited to a statement of consistency. While much future modelling work remains to be done to improve the tracing of mergers in the SFR/ L_{AGN} plane, results from these current models are consistent with mergers spending considerable time in the general area of the ‘correlation line’ of Fig. 4.

5.3. Connections between global star-formation and AGN activity

The existence of two regimes in the relationships between host SF and AGN activity suggests that there exists one or more key processes which modulate both star-formation and accretion

onto the nuclear black hole. Since the two regimes are distinguished by AGN luminosity, this implies that the main mode of AGN fueling changes between low and high luminosity AGNs. By this, we mean that the principal process (or family of processes) that drive the growth of AGNs is fundamentally different between the two regimes in AGN luminosity, and these two sorts of processes differ in their connection to global SF.

Some insight into the processes that govern fueling at lower AGN luminosities comes from the well-studied population of local Seyfert galaxies, which account for most of the low and moderate luminosity AGNs in the local Universe (e.g., Simkin et al. 1980). Seyfert host galaxies tend to be massive disks with substantial spheroids, though some fraction are also in more elliptical hosts (Kauffmann et al. 2003, 2007; Schawinski et al. 2010). While on-going major mergers are found among Seyferts, they account for only a minority of hosts. The statistics of galaxy morphology and color among local Seyferts strongly disfavors a major merger origin for the majority of local AGNs, since the big, stable disks in such galaxies could not have undergone a recent merger event.

A plausible scenario, supported by such studies of the structure and environment of local Seyfert galaxies is that SMBH fueling in low-luminosity AGNs is driven mostly by stochastic infall of gas from the circumnuclear region of the host galaxy and bears little connection to the extended SFR in the host (Kauffmann & Heckman 2009). Circumnuclear gas is replenished by several ‘secular’ processes that operate on the many galaxy-wide dynamical timescales. The large differences between active periods of low-luminosity accretion and such long replenishment times disconnects the nature of gas in the galaxy at large and the more rapid.

We find that the hosts of low luminosity AGNs are slightly, but measurably, different from inactive galaxies. Santini et al. (2012) find that they have a slightly enhanced *mean* SFR compared to normal galaxies of the same mass and in Fig. 3, we show that AGN hosts have warmer than typical FIR colors. This implies that, while the SFR in these hosts is not explicitly connected to AGN fueling, there is a preference for AGNs to lie in galaxies that are currently forming stars. The small shift to warmer colors among AGNs could be explained if AGNs are preferentially in star-forming galaxies that have more central or circumnuclear SF, where ambient gas densities and dust temperatures may be a bit higher than in the outskirts of galaxies. It may be that the processes that trigger bursts of SF in the centers of galaxies may also be related to gas inflow to the nucleus, though not in a synchronised manner. This is supported by high-resolution simulations of gas inflow to the inner few parsecs in disk galaxies (Hopkins & Quataert 2010).

Luminous AGNs ($L_{\text{AGN}} > L_{\text{AGN}}^c$), on the other hand, are fueled by rapid nuclear inflow of gas associated with major mergers of gas-rich galaxies (Menci et al. 2008; Volonteri et al. 2003; Hopkins & Beacom 2006; Hopkins et al. 2008b; Somerville et al. 2008). Since they also inspire strong star-bursts, major mergers are a good candidate for a galaxy-wide process that directly correlates AGN accretion and host star-formation. In a sense, the merger-driven starburst-QSO connection may be thought of as a scaled up version of the SF–accretion relationship that may more commonly found among low-luminosity AGN, since in mergers the total SFR of the host galaxy is dominated by the nuclear starburst.

5.4. The role of major mergers at high redshift

Turning now to $z \gtrsim 1$, our results show that the correlation between SF and AGN luminosity weakens or disappears at these redshifts. We proceed with an interpretation taking the points as they are measured, but caution that the interpretation is subject to the uncertainties associated with the measurement of L_{60} for the most luminous AGNs.

Guided by our explanations in the above discussion of low redshift trends, we can develop a couple of explanations for the flattening of the high redshift relationship. It may be that the secular processes active in low-redshift Seyferts are capable of fueling most high luminosity AGNs as well. Several studies have established that gas-rich, turbulent disks are common among massive galaxies at high redshift, due to high inflow rates of cold gas (Erb et al. 2006; Förster Schreiber et al. 2006, 2009). In such disks, a greater turbulent viscosity leads to a higher SMBH accretion rate (Bournaud et al. 2011a,b), and possibly more frequent high Eddington-ratio bursts, without necessarily producing a direct connection between accretion rate and SFR. If greater turbulent accretion can fuel luminous AGNs, the role of mergers could be eclipsed at high redshift by fueling through such secular means.

Having said this, current simulations still do not have the resolution to link large stochastic bursts of accretion to enhanced secular inflow, so the idea developed above is not strongly motivated by theory. If, instead, luminous AGNs at all redshifts are attributed to major mergers, then the lack of a correlation at high redshifts could occur if a regime of SF-AGN synchronisation, associated locally with the final coalescence of major gas-rich mergers, is lost among distant galaxies. This may happen if, for e.g. the interval of time between major mergers at high redshifts is short compared to the timescale of peak accretion, as cosmological simulations seem to suggest.

5.5. Implications for black hole-galaxy coevolution

If the correlation between L_{60} and L_{AGN} is indeed due to a dominant role of mergers among luminous AGNs, as supported by studies of local and low redshift populations, our results suggest a change in the relevance or nature of major galaxy mergers as drivers of AGN-galaxy co-evolution at high redshifts. We turn now to the implications of this in the context of galaxy evolution.

The most popular explanation for the form and tightness of the well-known local $M_{BH}-\sigma$ relationship is that most black hole growth occurs in major mergers, where both the galaxy and the SMBH grow in lock-step. These high luminosity, high accretion-rate phases of SMBH growth are visible in their end stages as QSOs and evolutionary models of SMBH growth by mergers can explain simultaneously the form and evolution of empirical SMBH mass functions, QSO luminosity functions, merger and red galaxy density functions, clustering, and the X-ray background (Hopkins et al. 2008b,a; Somerville et al. 2008).

Our results suggest that at low- z , most massive BH growth occurs in mergers or other possible processes that subject the host to violent relaxation. This maintains and tightens the massive end of local SMBH scaling relations.

At high- z , mergers may be less important. Many studies show that high- z galaxies are quite different from local ones. SF galaxies typically have large gas fractions and high turbulent line-widths (Genzel et al. 2008; Förster Schreiber et al. 2009; Daddi et al. 2010; Tacconi et al. 2010). Such galaxies can have a high duty-cycle of unstable modes (clumps, bars, grand

spirals) which can strongly torque gas. In addition, the larger magnitude of turbulent viscosity compared to local settled gas disks also plausibly leads to greater net ‘secular’ inflow to the nucleus. Simulations suggest that sustained inflow rates are enhanced at these redshifts (Bournaud et al. 2011a).

It is unclear if this larger net accretion rate to the nuclear regions translates into an increase in the frequency of low-luminosity AGNs, as suggested by Bournaud et al. (2011a), or a boost across the board in the density of AGNs at all luminosities. The flattening of the faint-end slope with redshift from X-ray luminosity functions (Silverman et al. 2008; Aird et al. 2010) supports the latter explanation. If so, the flat $L_{60}-L_{AGN}$ trend at $z > 1$ suggests that the role of mergers in fueling high luminosity AGNs may be replaced by global disk instabilities in gas-rich galaxies, which effectively removes the synchronisation between AGN accretion rate and SFR inherent to major mergers. Secular processes, which are important for low-luminosity AGNs at low redshifts, become dominant at all AGN luminosities at $z > 1$.

Regardless of the mechanism, our results suggest that the lock-step growth of stellar mass and galaxy properties becomes effectively decoupled from the growth of the black hole at higher redshifts. Most models of SMBH-galaxy co-evolution require that black holes grow in concert with their host galaxy (at least its spheroidal component). However, at the redshifts where both the stellar content and black holes in massive galaxies are put into place, the correlation between SMBH and galaxy growth seems to weaken or disappear. This suggests that alternative ideas are needed to tie BH growth to galaxy growth, in order to yield the tight $M_{BH}-\sigma$ relation seen today. Possible ideas are a strong role for feedback-regulated BH growth, coupled with a short lag between BH and bulge growth (Hopkins et al. 2009), or perhaps pure statistical evolution of both components in a hierarchical merging context (Jahnke & Macciò 2011).

6. Summary

We have explored the variation of the mean far-IR luminosity of X-ray selected active galaxies with AGN luminosity and obscuration, using deep X-ray and Herschel/PACS datasets in three key extragalactic survey fields: GOODS-S, GOODS-N and COSMOS. Through the combination of both narrow+deep and wide+shallow surveys, redshift binning and the inclusion of stacked measurements for FIR-undetected subsamples, we avoid the effects of Malmquist bias which can produce incorrect correlations between SFR and AGN properties in FIR detected samples taken only from wide+shallow surveys.

We gauge the importance of hot dust emission from the active nucleus at FIR wavelengths, using a suite of empirical AGN SEDs and SEDs of star-forming galaxies, chosen to cover most of the range of SED shapes expected for these two galaxy components. We compare the observed-frame MIR and FIR colors of AGNs and IR-bright inactive (X-ray undetected) galaxies in bins of redshift, finding that active galaxies generally span roughly the same color range as inactive galaxies at FIR wavelengths, though with a small tendency to host warmer FIR SEDs. We also demonstrate that a small minority of AGNs, typically the most luminous ones, are dominated by hot dust emission from the active nucleus.

After appropriately combining measurements from all three fields, we find characteristic trends between AGN luminosity and FIR luminosity L_{60} . Low-luminosity AGNs display essentially no relationship between global star-formation rate, as traced by FIR luminosity, and the luminosity of the active nucleus. Instead, the L_{60} of such AGNs increases with redshift as

expected from studies of the SFR evolution of inactive massive galaxies. Black hole fueling in these systems is probably dominated by secular processes related to gas inflow and momentum transfer in galaxy disks and is unrelated to the overall growth of the host.

On the other hand, luminous AGNs ($L_{AGN} > 10^{44.8}$ erg s⁻¹) at low and moderate redshift ($z < 1$) show a strong correlation between SFR and nuclear luminosity, implying a close relationship between the growth of the stellar component of the host galaxy and the growth of the SMBH. We interpret this as evidence for the importance of gas-rich major mergers in fueling high accretion phases in AGNs at these redshifts, consistent with the results of modern hydrodynamic simulations.

At higher redshifts ($z > 1$), we find that the correlation flattens or disappears, implying a weaker connection between galaxy and black hole growth. This suggests that the role of major mergers as drivers of black hole-galaxy co-evolution evolves with redshift. If so, this has important implications for co-evolutionary models and the evolution of the M_{BH} - σ relationship.

We find very little dependence between the mean FIR luminosity and X-ray obscuring column N_H in X-ray selected AGNs, over five orders of magnitude in N_H . The population of obscured AGNs do not distinguish themselves in terms of their current SFR and various mechanisms are may be responsible for obscuring the nuclear X-ray emission of AGNs, with some certainly unrelated to global star-formation in the host galaxy.

Acknowledgements. We thank Marta Volonteri for valuable discussions. PACS has been developed by a consortium of institutes led by MPE (Germany) and including UVIE (Austria); KU Leuven, CSL, IMEC (Belgium); CEA, LAM (France); MPIA (Germany); INAF-IFSI/OAA/OAP/OAT, LENS, SISSA (Italy); IAC (Spain). This development has been supported by the funding agencies BMVIT (Austria), ESA-PRODEX (Belgium), CEA/CNES (France), DLR (Germany), ASI/INAF (Italy), and CICYT/MCYT (Spain). FB acknowledges support from Financiamiento Basal, CONICYT-Chile FONDECYT 1101024 and fondap-cata 15010003, and Chandra X-ray Center grant SAO SP1-12007B (F.E.B.)

References

- Aird, J., Nandra, K., Laird, E. S., et al. 2010, *MNRAS*, 401, 2531
 Alexander, D. M., Bauer, F. E., Brandt, W. N., et al. 2003, *AJ*, 126, 539
 Alexander, D. M., Brandt, W. N., Smail, I., et al. 2008, *AJ*, 135, 1968
 Alonso-Herrero, A., Pérez-González, P. G., Rieke, G. H., et al. 2008, *ApJ*, 677, 127
 Assef, R. J., Kochanek, C. S., Ashby, M. L. N., et al. 2011, *ApJ*, 728, 56
 Bahcall, J. N., Kirhakos, S., Saxe, D. H., & Schneider, D. P. 1997, *ApJ*, 479, 642
 Bauer, F. E., Alexander, D. M., Brandt, W. N., et al. 2004, *AJ*, 128, 2048
 Berta, S., Magnelli, B., Nordon, R., et al. 2011, *A&A*, 532, A49
 Bethermin, M., Dole, H., Beelen, A., & Aussel, H. 2010, *VizieR Online Data Catalog*, 3512, 29078
 Bonfield, D. G., Jarvis, M. J., Hardcastle, M. J., et al. 2011, *MNRAS*, 416, 13
 Bongiorno, A., Zamorani, G., Gavignaud, I., et al. 2007, *A&A*, 472, 443
 Bournaud, F., Dekel, A., Teyssier, R., et al. 2011a, *ApJ*, 741, L33
 Bournaud, F., Juneau, S., Le Floch, E., et al. 2011b, *ArXiv e-prints*
 Boyle, B. J. & Terlevich, R. J. 1998, *MNRAS*, 293, L49
 Brusa, M., Civano, F., Comastri, A., et al. 2010, *ApJ*, 716, 348
 Brusa, M., Fiore, F., Santini, P., et al. 2009, *A&A*, 507, 1277
 Cameron, E. 2011, *PASA*, 28, 128
 Canalizo, G. & Stockton, A. 2001, *ApJ*, 555, 719
 Cappelluti, N., Brusa, M., Hasinger, G., et al. 2009, *A&A*, 497, 635
 Chary, R. & Elbaz, D. 2001, *ApJ*, 556, 562
 Cisternas, M., Jahnke, K., Inskip, K. J., et al. 2011, *ApJ*, 726, 57
 Coil, A. L., Georgakakis, A., Newman, J. A., et al. 2009, *ApJ*, 701, 1484
 Coppin, K. E. K., Swinbank, A. M., Neri, R., et al. 2008, *MNRAS*, 389, 45
 Cowie, L. L., Barger, A. J., Bautz, M. W., Brandt, W. N., & Garmire, G. P. 2003, *ApJ*, 584, L57
 Cox, T. J., Dutta, S. N., Di Matteo, T., et al. 2006, *ApJ*, 650, 791
 Croom, S. M., Smith, R. J., Boyle, B. J., et al. 2004, *MNRAS*, 349, 1397
 Cusumano, G., La Parola, V., Segreto, A., et al. 2009, *VizieR Online Data Catalog*, 3510, 9048
 Daddi, E., Bournaud, F., Walter, F., et al. 2010, *ApJ*, 713, 686
 Daddi, E., Dickinson, M., Morrison, G., et al. 2007, *ApJ*, 670, 156
 Dale, D. A. & Helou, G. 2002, *ApJ*, 576, 159
 Davies, R. I., Müller Sánchez, F., Genzel, R., et al. 2007, *ApJ*, 671, 1388
 Davis, M., Guhathakurta, P., Konidaris, N. P., et al. 2007, *ApJ*, 660, L1
 Diamond-Stanic, A. M. & Rieke, G. H. 2011, *ArXiv e-prints*
 Dickinson, M., Giavalisco, M., & GOODS Team. 2003, in *The Mass of Galaxies at Low and High Redshift*, ed. R. Bender & A. Renzini, 324
 Dunlop, J. S., McLure, R. J., Kukula, M. J., et al. 2003, *MNRAS*, 340, 1095
 Efstathiou, A. & Rowan-Robinson, M. 1995, *MNRAS*, 273, 649
 Erb, D. K., Steidel, C. C., Shapley, A. E., et al. 2006, *ApJ*, 646, 107
 Ferrarese, L. & Ford, H. 2005, *Space Sci. Rev.*, 116, 523
 Ferrarese, L. & Merritt, D. 2000, *ApJ*, 539, L9
 Ferrarese, L., Pogge, R. W., Peterson, B. M., et al. 2001, *ApJ*, 555, L79
 Fiore, F., Brusa, M., Cocchia, F., et al. 2003, *A&A*, 409, 79
 Fontanot, F., De Lucia, G., Monaco, P., Somerville, R. S., & Santini, P. 2009, *MNRAS*, 397, 1776
 Förster Schreiber, N. M., Genzel, R., Bouché, N., et al. 2009, *ApJ*, 706, 1364
 Förster Schreiber, N. M., Genzel, R., Lehnert, M. D., et al. 2006, *ApJ*, 645, 1062
 Fritz, J., Franceschini, A., & Hatziminaoglou, E. 2006, *MNRAS*, 366, 767
 Gandhi, P., Horst, H., Smette, A., et al. 2009, *A&A*, 502, 457
 Gebhardt, K., Bender, R., Bower, G., et al. 2000, *ApJ*, 539, L13
 Genzel, R., Burkert, A., Bouché, N., et al. 2008, *ApJ*, 687, 59
 Genzel, R., Lutz, D., Sturm, E., et al. 1998, *ApJ*, 498, 579
 Granato, G. L. & Danese, L. 1994, *MNRAS*, 268, 235
 Greene, J. E., Zakamska, N. L., Liu, X., Barth, A. J., & Ho, L. C. 2009, *ApJ*, 702, 441
 Grogin, N. A., Conselice, C. J., Chatzichristou, E., et al. 2005, *ApJ*, 627, L97
 Gültekin, K., Richstone, D. O., Gebhardt, K., et al. 2009, *ApJ*, 698, 198
 Guyon, O., Sanders, D. B., & Stockton, A. 2006, *ApJS*, 166, 89
 Haas, M., Chini, R., Meisenheimer, K., et al. 1998, *ApJ*, 503, L109
 Hasinger, G., Miyaji, T., & Schmidt, M. 2005, *A&A*, 441, 417
 Hatziminaoglou, E., Omont, A., Stevens, J. A., et al. 2010, *A&A*, 518, L33+
 Hopkins, A. M. & Beacom, J. F. 2006, *ApJ*, 651, 142
 Hopkins, P. F., Cox, T. J., Kereš, D., & Hernquist, L. 2008a, *ApJS*, 175, 390
 Hopkins, P. F., Hernquist, L., Cox, T. J., & Kereš, D. 2008b, *ApJS*, 175, 356
 Hopkins, P. F., Hernquist, L., Martini, P., et al. 2005, *ApJ*, 625, L71
 Hopkins, P. F., Murray, N., & Thompson, T. A. 2009, *MNRAS*, 398, 303
 Hopkins, P. F. & Quataert, E. 2010, *MNRAS*, 407, 1529
 Jahnke, K. & Macciò, A. V. 2011, *ApJ*, 734, 92
 Jahnke, K., Sánchez, S. F., Wisotzki, L., et al. 2004, *ApJ*, 614, 568
 Kauffmann, G. & Heckman, T. M. 2009, *MNRAS*, 397, 135
 Kauffmann, G., Heckman, T. M., Budavári, T., et al. 2007, *ApJS*, 173, 357
 Kauffmann, G., Heckman, T. M., Tremonti, C., et al. 2003, *MNRAS*, 346, 1055
 Kocevski, D. D., Faber, S. M., Mozena, M., et al. 2012, *ApJ*, 744, 148
 Koss, M., Mushotzky, R., Veilleux, S., & Winter, L. 2010, *ApJ*, 716, L125
 Lotz, J. M., Jonsson, P., Cox, T. J., et al. 2011, *ApJ*, 742, 103
 Luo, B., Bauer, F. E., Brandt, W. N., et al. 2008, *ApJS*, 179, 19
 Luo, B., Brandt, W. N., Xue, Y. Q., et al. 2010, *ApJS*, 187, 560
 Lutz, D., Mainieri, V., Rafferty, D., et al. 2010, *ApJ*, 712, 1287
 Lutz, D., Poglitsch, A., Altieri, B., et al. 2011, *A&A*, 532, A90
 Lutz, D., Sturm, E., Tacconi, L. J., et al. 2008, *ApJ*, 684, 853
 Magorrian, J., Tremaine, S., Richstone, D., et al. 1998, *AJ*, 115, 2285
 Mainieri, V., Bongiorno, A., Merloni, A., et al. 2011, *A&A*, 535, A80
 Maiolino, R., Shemmer, O., Imanishi, M., et al. 2007, *A&A*, 468, 979
 Marconi, A. & Hunt, L. K. 2003, *ApJ*, 589, L21
 Martini, P. & Weinberg, D. H. 2001, *ApJ*, 547, 12
 Menci, N., Fiore, F., Puccetti, S., & Cavaliere, A. 2008, *ApJ*, 686, 219
 Mor, R. & Netzer, H. 2012, *MNRAS*, 420, 526
 Mor, R., Netzer, H., & Elitzur, M. 2009, *ApJ*, 705, 298
 Mullaney, J. R., Alexander, D. M., Goulding, A. D., & Hickox, R. C. 2011, *MNRAS*, 414, 1082
 Mullaney, J. R., Pannella, M., Daddi, E., et al. 2012, *MNRAS*, 419, 95
 Nenkova, M., Ivezić, Ž., & Elitzur, M. 2002, *ApJ*, 570, L9
 Netzer, H. 2009, *MNRAS*, 399, 1907
 Netzer, H., Lutz, D., Schweitzer, M., et al. 2007, *ApJ*, 666, 806
 Netzer, H. & Trakhtenbrot, B. 2007, *ApJ*, 654, 754
 Noeske, K. G., Weiner, B. J., Faber, S. M., et al. 2007, *ApJ*, 660, L43
 Nordon, R., Lutz, D., Genzel, R., et al. 2012, *ApJ*, 745, 182
 Omont, A., Beelen, A., Bertoldi, F., et al. 2003, *A&A*, 398, 857
 Page, M. 2011, in *The Starburst-AGN Connection under the Multiwavelength Limelight*
 Page, M. J., Stevens, J. A., Ivison, R. J., & Carrera, F. J. 2004, *ApJ*, 611, L85
 Page, M. J., Stevens, J. A., Mittaz, J. P. D., & Carrera, F. J. 2001, *Science*, 294, 2516
 Pérez-González, P. G., Rieke, G. H., Villar, V., et al. 2008, *ApJ*, 675, 234
 Pier, E. A. & Krolik, J. H. 1992, *ApJ*, 401, 99
 Pilbratt, G. L., Riedinger, J. R., Passvogel, T., et al. 2010, *A&A*, 518, L1

- Poglitisch, A., Waelkens, C., Geis, N., et al. 2010, *A&A*, 518, L2
 Polletta, M., Tajer, M., Maraschi, L., et al. 2007, *ApJ*, 663, 81
 Priddey, R. S., Isaak, K. G., McMahon, R. G., & Omont, A. 2003, *MNRAS*, 339, 1183
 Rosario, D. J., Mozena, M., Wuyts, S., et al. 2011, *ArXiv e-prints*
 Rowan-Robinson, M. 1995, *MNRAS*, 272, 737
 Salvato, M., Hasinger, G., Ilbert, O., et al. 2009, *ApJ*, 690, 1250
 Sanders, D. B. & Mirabel, I. F. 1996, *ARA&A*, 34, 749
 Sanders, D. B., Soifer, B. T., Elias, J. H., et al. 1988, *ApJ*, 325, 74
 Santini, P., Fontana, A., Grazian, A., et al. 2009, *A&A*, 504, 751
 Santini, P., Rosario, D. J., Shao, L., et al. 2012, *A&A*, 540, A109
 Schartmann, M., Meisenheimer, K., Camenzind, M., et al. 2008, *A&A*, 482, 67
 Schawinski, K., Urry, C. M., Virani, S., et al. 2010, *ApJ*, 711, 284
 Schweitzer, M., Groves, B., Netzer, H., et al. 2008, *ApJ*, 679, 101
 Schweitzer, M., Lutz, D., Sturm, E., et al. 2006, *ApJ*, 649, 79
 Scoville, N., Aussel, H., Brusa, M., et al. 2007, *ApJS*, 172, 1
 Shao, L., Lutz, D., Nordon, R., et al. 2010, *A&A*, 518, L26+
 Shi, Y., Rieke, G. H., Hines, D. C., et al. 2005, *ApJ*, 629, 88
 Shi, Y., Rieke, G. H., Ogle, P., Jiang, L., & Diamond-Stanic, A. M. 2009, *ApJ*, 703, 1107
 Silverman, J. D., Green, P. J., Barkhouse, W. A., et al. 2008, *ApJ*, 679, 118
 Silverman, J. D., Lamareille, F., Maier, C., et al. 2009, *ApJ*, 696, 396
 Silverman, J. D., Mainieri, V., Salvato, M., et al. 2010, *ApJS*, 191, 124
 Simkin, S. M., Su, H. J., & Schwarz, M. P. 1980, *ApJ*, 237, 404
 Somerville, R. S., Hopkins, P. F., Cox, T. J., Robertson, B. E., & Hernquist, L. 2008, *MNRAS*, 391, 481
 Springel, V. 2005, *MNRAS*, 364, 1105
 Stevens, J. A., Page, M. J., Ivison, R. J., et al. 2005, *MNRAS*, 360, 610
 Tacconi, L. J., Genzel, R., Neri, R., et al. 2010, *Nature*, 463, 781
 Tozzi, P., Gilli, R., Mainieri, V., et al. 2006, *A&A*, 451, 457
 Tremaine, S., Gebhardt, K., Bender, R., et al. 2002, *ApJ*, 574, 740
 Ueda, Y., Akiyama, M., Ohta, K., & Miyaji, T. 2003, *ApJ*, 598, 886
 Urrutia, T., Lacy, M., & Becker, R. H. 2008, *ApJ*, 674, 80
 Veilleux, S., Kim, D.-C., Rupke, D. S. N., et al. 2009, *ApJ*, 701, 587
 Volonteri, M., Haardt, F., & Madau, P. 2003, *ApJ*, 582, 559
 Wild, V., Heckman, T., & Charlot, S. 2010, *MNRAS*, 405, 933
 Wild, V., Kauffmann, G., Heckman, T., et al. 2007, *MNRAS*, 381, 543
 Wuyts, S., Cox, T. J., Hayward, C. C., et al. 2010, *ApJ*, 722, 1666
 Xue, Y. Q., Brandt, W. N., Luo, B., et al. 2010, *ApJ*, 720, 368

Appendix A: FIR luminosities: detection, stacking and measurement

As a direct tracer of the FIR emission we concentrate on the mean luminosity $\nu L_\nu(60\mu\text{m})$, estimated at a rest-frame wavelength of $60\mu\text{m}$. This choice is a compromise between a wavelength long enough to avoid most of the AGN contamination (see discussion below) and at the same time short enough to be sampled by PACS $160\mu\text{m}$ observations even at the highest redshifts considered in this work.

To preclude any assumptions about the SED shape, we computed $\nu L_\nu(60\mu\text{m})$ through a log-linear interpolation of PACS fluxes, after converting them to luminosities following the approach of Shao et al. (2010). For the GOODS-S dataset, which includes $70\mu\text{m}$ observations as well, we interpolated between the two PACS bands bracketing rest-frame $60\mu\text{m}$. We checked that wider wavelength coverage in GOODS-S (the addition of $70\mu\text{m}$ observations) does not introduce any bias in the analysis: when interpolating rest-frame $60\mu\text{m}$ luminosity only from 100 and $160\mu\text{m}$ PACS photometry, our results remain unchanged, and individual $\nu L_\nu(60\mu\text{m})$ do not differ by more than 50%.

We also explored fitting PACS fluxes with a typical IR template (e.g. from Chary & Elbaz 2001 or Dale & Helou 2002 libraries) to derive $\nu L_\nu(60\mu\text{m})$. We found differences by a few tens per cent (only in 15% of the bins is the difference larger than 50%), but the global picture is unaffected. Therefore, we adopt the simple interpolated $\nu L_\nu(60\mu\text{m})$ estimate throughout, making no assumptions on the detailed SED shape.

For sources fully detected (i.e. detected in both PACS bands used to interpolate $60\mu\text{m}$ luminosity) we used the corresponding

fluxes and computed individual $\nu L_\nu(60\mu\text{m})$. For PACS sources that were completely undetected in both bands, we computed average fluxes by stacking in a given L_X and redshift interval. We stacked at the X-ray positions on PACS residual maps using the Bethermin et al. (2010) libraries. The use of residual maps, from which all detected objects were removed, avoids contamination by nearby brighter sources. PSF photometry was performed on the final stacked images. For each PACS band j , we then averaged these stacked fluxes with individual fluxes of partially detected objects (i.e. detected only in band j but not in the other one), weighting by the number of sources. These stacked and averaged fluxes in each band are used to get $\nu L_\nu^{STACK}(60\mu\text{m})$, in the same fashion as for the fully detected sources.

The final $60\mu\text{m}$ luminosity in each L_X and redshift interval is computed by averaging over the linear luminosities of detections and non-detections, weighted by the number of sources. Only bins with more than 3 sources are used in our analysis.

Errors on the infrared luminosity were obtained by bootstrapping, in similar fashion as many current studies (Shao et al. 2010; Mullaney et al. 2012; Santini et al. 2012). A set of N sources, where N is equal to the number of sources per bin in L_X and redshift, is randomly chosen 100 times among detections and non-detections (allowing repetitions), and a $\nu L_\nu(60\mu\text{m})$ is computed per each iteration. The standard deviation of the obtained $\nu L_\nu(60\mu\text{m})$ values gives the error on the average $60\mu\text{m}$ luminosity in each bin. The error bars thus account for both measurement errors and the error on the population distribution. They do not, however, account for cosmic variance.

Appendix B: Combination across fields

To reduce scatter and the effects of cosmic variance, we combine the estimates of the average $\nu L_\nu(60\mu\text{m})$ in each bin in redshift and X-ray luminosity from all three fields into one mean number for each bin.

The PACS maps in each of the fields differ in depth and area. Therefore, we begin by comparing the estimates of $\nu L_\nu(60\mu\text{m})$ in all three fields against redshift, as a simple test to ensure that the mean measurements in all three fields are in fact compatible. In the three upper panels of Fig. B.1, we plot the mean $\nu L_\nu(60\mu\text{m})$ from AGNs in each of the three fields separately. The points are colored by bins in X-ray luminosity. At a glance, one may gather that both the measurements and their redshift evolution in all three fields are very comparable.

In the lower three panels of Fig. B.1, we plot separately the $\nu L_\nu(60\mu\text{m})$ of PACS detected AGNs and those derived from stacks of the undetected AGNs. In addition, we have plotted the approximate rest-frame $60\mu\text{m}$ luminosity limit as a function of redshift, derived from a log-linear interpolation of the 3σ PACS detection limits at 100 and $160\mu\text{m}$ for each field. These luminosity limits match reasonably well the lower envelope of the PACS detected AGNs in the Figure. The COSMOS detections are more luminous than those in the GOODS fields both at the luminosity limit, due to the significantly shallower PACS imaging, as well as at the upper end, because the larger area of the COSMOS field ($5\times$ larger than the GOODS fields combined) brings in more of the rare, very FIR luminous galaxies into the sample. The stacked points can be up to an order of magnitude fainter than the PACS luminosity limit.

Due to the differences in the depth and noise properties of the PACS images in the three different fields, combining the data at the level of the maps poses difficulties. On the other hand, the measurements of FIR luminosity in each of the three fields show consistent values and behavior with redshift and L_X . Therefore

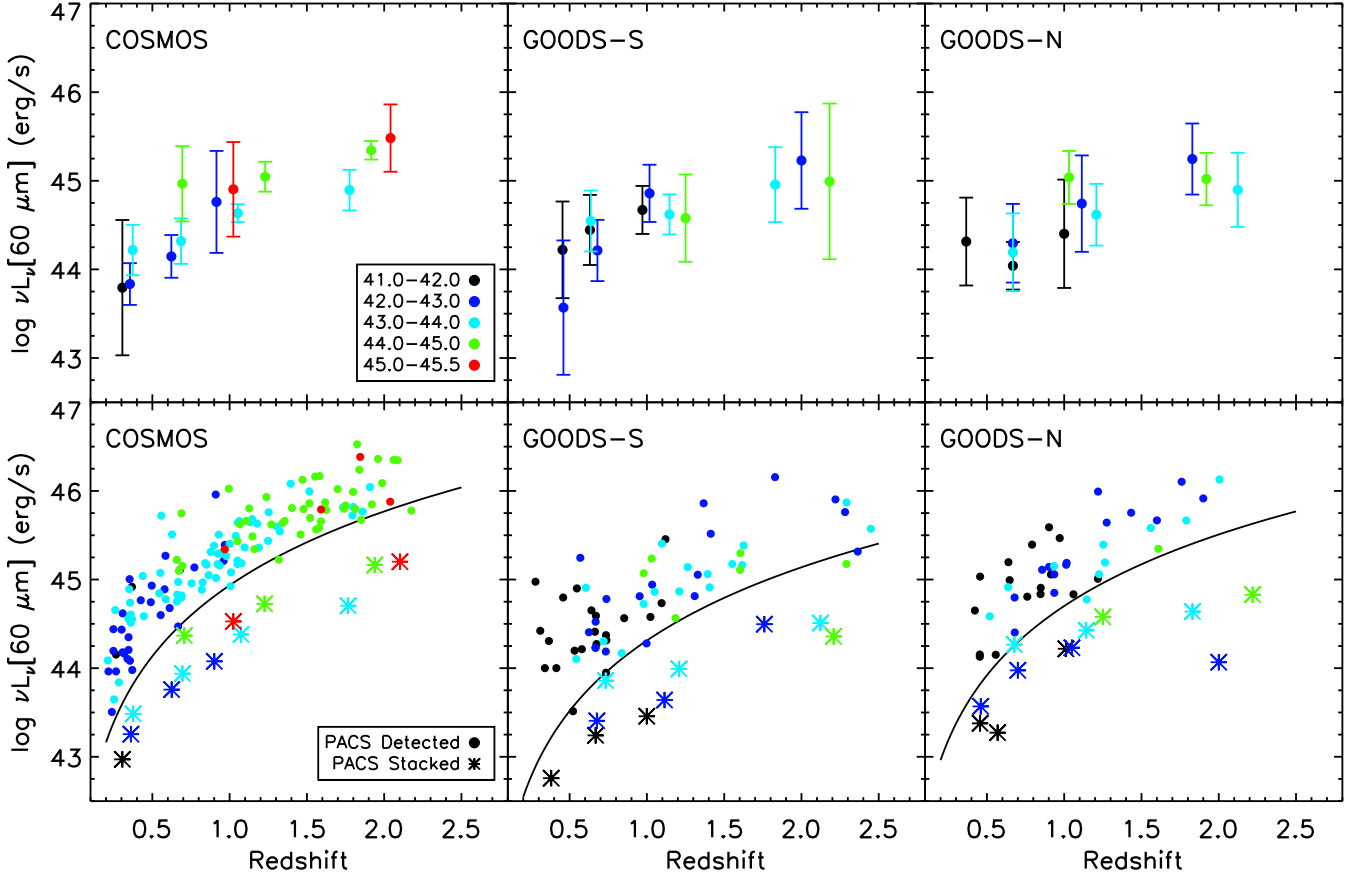


Fig. B.1. $\nu L_{\nu}(60\mu\text{m})$ as a function of redshift for X-ray AGNs in the individual COSMOS, GOODS-S and GOODS-N fields. The points in all panels are colored by logarithmic bins in hard band X-ray luminosity (L_X), as shown. The upper panels show the mean L_{60} estimated by combining fluxes from PACS detections and stacks. Note the consistency across all fields between the values and variation with redshift of the mean measurements. The lower panels show individual PACS detected AGNs and the stacked points for PACS undetected AGNs (in bins of redshift and L_X). The solid black lines show the approximate 3σ $\nu L_{\nu}(60\mu\text{m})$ limit, derived from the flux limits of the 100 and 160 μm PEP photometry catalogs.

we combined *post-facto* the estimates of the mean $\nu L_{\nu}(60\mu\text{m})$ in each redshift and L_X bin. This was done by taking an average of the FIR luminosity in all three fields in each bin with a valid measurement, weighted by the inverse variance ($1/\text{err}^2$) derived from the errors on the mean FIR luminosity.